

Large-eddy simulation of transition to turbulence in a boundary layer developing spatially over a flat plate

By FRÉDÉRIC DUCROS, PIERRE COMTE
AND MARCEL LESIEUR

Institut de Mécanique de Grenoble, Laboratoire des Ecoulements Géophysiques et Industriels†, BP53, F-38041 Grenoble Cedex 9, France

(Received 6 February 1995 and in revised form 13 May 1996)

It is well known that subgrid models such as Smagorinsky's cannot be used for the spatially growing simulation of the transition to turbulence of flat-plate boundary layers, unless large-amplitude perturbations are introduced at the upstream boundary: they are over-dissipative, and the flow simulated remains laminar. This is also the case for the structure-function model (SF) of Métais & Lesieur (1992). In the present paper we present a sequel to this model, the filtered-structure-function (FSF) model. It consists of removing the large-scale fluctuations of the field before computing its second-order structure function. Analytical arguments confirm the superiority of the FSF model over the SF model for large-eddy simulations of weakly unstable transitional flows. The FSF model is therefore used for the simulation of a quasi-incompressible ($M_\infty = 0.5$) boundary layer developing spatially over an adiabatic flat plate, with a low level of upstream forcing. With the minimal resolution $650 \times 32 \times 20$ grid points covering a range of streamwise Reynolds numbers $Re_{x_1} \in [3.4 \times 10^5, 1.1 \times 10^6]$, transition is obtained for 80 hours of time-processing on a CRAY 2 (whereas DNS of the whole transition takes about ten times longer). Statistics of the LES are found to be in acceptable agreement with experiments and empirical laws, in the laminar, transitional and turbulent parts of the domain. The dynamics of low-pressure and high-vorticity distributions is examined during transition, with particular emphasis on the neighbourhood of the critical layer (defined here as the height of the fluid travelling at a speed equal to the phase speed of the incoming Tollmien–Schlichting waves). Evidence is given that a subharmonic-type secondary instability grows, followed by a purely spanwise (i.e. time-independent) mode which yields peak-and-valley splitting and transition to turbulence. In the turbulent region, flow visualizations and local instantaneous profiles are provided. They confirm the presence of low- and high-speed streaks at the wall, weak hairpins stretched by the flow and bursting events. It is found that most of the vorticity is produced in the spanwise direction, at the wall, below the high-speed streaks. Isosurfaces of eddy viscosity confirm that the FSF model does not perturb transition much, and acts mostly in the vicinity of the hairpins.

† Institut National Polytechnique de Grenoble (INPG), Université Joseph Fourier (UJF), et Centre National de la Recherche Scientifique (CNRS).

1. Introduction

The fundamental problem of transition to turbulence is still a challenge in computational fluid dynamics, even for very simple flows like incompressible boundary layers over a flat plate (see Kleiser & Zang 1991, for a review). Indeed, although direct numerical simulations (DNS) prove to be a very efficient tool in streamwise-periodic cases (temporal boundary layers, see Spalart & Yang 1987, and Spalart 1988), spatially developing flows require such tremendous resolution that one usually chooses to simulate just the earliest stages of transition (Thumm, Wolz & Fasel 1989; Fasel & Konzelman 1990; Kleiser & Zang 1991; Joslin, Streett & Chang 1993). Recently Rai & Moin (1993) performed a direct numerical simulation of the complete transition of a spatially growing boundary layer using several grids (a coarse one in the transitional region, a fine one in the turbulent region and another coarse grid to accommodate the outlet conditions) and a relatively high level of perturbations (the levels of the r.m.s. velocities are about 2.75% of the free-stream velocities at the leading edge). Although they prove that such a DNS is possible, the cost is still very high: 800 hours of a CRAY YMP. Since atmospheric or wind-tunnel residual turbulence is generally less intense, DNS in a more realistic situation should be more expensive.

On the other hand, large-eddy simulation (LES) can be a more affordable alternative, provided the subgrid-scale (SGS) model used

dissipates fluctuations in the smallest resolved scales at an acceptable rate, is able to turn itself off in the absence of small-scale fluctuations.

As far as the first point is concerned, Smagorinsky's (1963) model has been proved to behave well in a fully turbulent channel flow since Deardorff's (1970) pioneering simulations, with the help of an empirical damping function at the wall and a reduction by half of the model's constant with respect to the value predicted in the only case tractable analytically, i.e. isotropic turbulence following an infinite Kolmogorov cascade. These simulations were repeated at higher resolution by Moin & Kim (1982), who showed that wall turbulence is dominated by hairpin-like vortices stretched by the mean flow.

However, it soon became obvious that Smagorinsky's model was too dissipative during the early stages of transition to permit simulation at a significantly lower resolution than in DNS. One way around this was to increase the level of upstream forcing, in order to overwhelm the model. Transition then occurs quicker, by-passing the stage during which instabilities amplify exponentially mode by mode as predicted by linear theories (*by-pass transition*, Voke & Yang 1993, with upstream forcing of turbulent intensity 6%).

Another solution, advocated here, is to use a model which meets better the second requirement mentioned above. This is the case for the *spectral models* (see Lesieur 1990) based upon the concept of *spectral eddy viscosity* introduced by Kraichnan (1976). In the case of incompressible isotropic turbulence, these *spectral models* define eddy viscosities proportional to $[E(k_C, t)/k_C]^{1/2}$, in which $E(k_C, t)$ stands for the kinetic-energy spectrum at the cut-off wavenumber k_C . They therefore remain strictly zero as long as $E(k_C, t)$ is zero, that is, roughly speaking, until small-scale transition. In the most elaborate version – the *spectral-cusp model* – the coefficient of proportionality is a function of the ratio k/k_C . This non-dimensional function $v_t^+(k/k_C)$ remains constant (*plateau*) for small values of k/k_C and exhibits a rising *cusp* when k is close to k_C , as predicted by two-point-closure stochastic theories. This cusp takes into account in particular, at least energetically, the effects of *backscatter* shown by many authors (see e.g. Domaradzki, Liu & Brachet 1993). In the plateau, the backscatter may be

shown to be negligible. The *spectral-cusp model* works well for flows which can be simulated by pseudo-spectral methods, e.g. isotropic turbulence (Chollet & Lesieur, 1981, Lesieur & Rogallo, 1989), stratified turbulence (Batchelor, Canuto & Chasnov 1992), and mixing layers (Silvestrini, Comte & Lesieur 1995). Unfortunately, spectral eddy-viscosities are difficult to implement in boundary layers spatially developing on a wall, where there is only one direction of homogeneity (spanwise), which poses problems for the determination of the kinetic-energy spectrum at the cutoff when the spanwise dimension is not large enough.

Métais & Lesieur (1992) thus proposed the *structure-function model* (SF), which is an equivalent in the physical space of the *spectral model* without cusp. The kinetic-energy spectrum at the cutoff $E(k_C)$ is evaluated 'locally' in the physical space, through the second-order velocity structure function at each grid point averaged over the six closest neighbouring points. This model was shown to behave very well in isotropic turbulence (Métais & Lesieur 1992), where it produces, in decaying situations, a good Kolmogorov spectrum close to the cutoff. It also works well for the backward-facing step flow (Silveira *et al.* 1993), the spatially developing wake (Gonze 1993), and homogeneous rotating turbulence (Bartello, Métais & Lesieur 1994).

In the presence of strong shear as in boundary layers, only the contributions to the structure function which are perpendicular to the shear are considered. This four-point formulation of the SF model, introduced by Normand & Lesieur (1992), gave very good results in the case of high-Mach-number ($M_\infty = 4.5$) periodic boundary layers (Ducros, Comte & Lesieur 1995), for which the initially dominant instability (Mack's second mode) is inviscid and therefore strongly amplified: the model allowed reproduction of the results of DNS during the transitional period (Pruett & Zang 1992; Adams & Kleiser 1993), and furthermore could reach the turbulent regime, which would have been impossible in DNS at a comparable resolution. In the spatially developing case, encouraging results were obtained at Mach 5 in the transitional region, still using the structure-function model in its four-point formulation without any specific compressibility correction (Normand & Lesieur 1992).

However, for incompressible boundary layers, the SF model, either in its six-point or four-point formulation, is not really better than Smagorinsky's during the early stages of transition. This is because the local kinetic-energy spectrum $E_x(k_C)$ arising in the eddy viscosity, and computed in terms of the structure function as if the flow were isotropic, is in fact sensitive to large-scale fluctuations. More precisely, it will be shown in the present paper that it is when oblique modes start developing above the Tollmien-Schlichting waves that the SF eddy viscosity becomes too dissipative.

At this point, we point out that Germano *et al.* (1991) made Smagorinsky's model 'dynamic' by adjusting its constant locally after a double filtering. In order to remove singularities, averages of the model constant had to be made in planes parallel to the wall. They could simulate transition of a periodic incompressible channel flow with not too high a level of initial forcing (2% amplitude). With a resolution up to $48 \times 65 \times 64$ points, they obtained statistics coherent with DNS at higher resolution. We are not aware of dynamic-model applications to spatially developing boundary-layer simulations, such as those presented below.

In the filtered structure-function model presented here, we filter out the large-scale fluctuations of the flow with the aid of a third-order Laplacian discretized by second-order finite differences, before computing the second-order structure function. This new *filtered structure-function model* (FSF) is employed to simulate transition of a quasi-incompressible boundary layer (external Mach number $M_\infty = 0.5$) developing spatially over an adiabatic flat plate, with a low level of upstream forcing (less than

1% amplitude) and affordable resolution ($650 \times 32 \times 20$ points). In fact, our aim is to show the feasibility of LES for transition in an incompressible boundary layer over a flat plate. We use for that a compressible code developed by Normand & Lesieur (1992), at an external Mach number such that the flow close to the wall is quasi-incompressible: at $x_2^+ = 12$ (the production peak, see below), the velocity is $\approx 0.3U_\infty$, and the Mach number ≈ 0.15 . In a forthcoming paper, and in order to study the effects of compressibility, temporal and spatial simulations of a boundary layer at Mach 4.5 will be presented (see also Ducros 1995).

The paper is organized as follows: §2 presents the subgrid model, §3 the computational domain, and §4 the results of the simulations.

2. Subgrid-scale modelling

The compressible Navier–Stokes equation can be cast in the following pseudo-conservative form:

$$\frac{\partial \mathbf{U}}{\partial t} + \frac{\partial \mathbf{F}_1}{\partial x_1} + \frac{\partial \mathbf{F}_2}{\partial x_2} + \frac{\partial \mathbf{F}_3}{\partial x_3} = 0, \quad (2.1)$$

with

$$\mathbf{U} = {}^T(\rho, \rho u_1, \rho u_2, \rho u_3, \rho e), \quad (2.2)$$

ρe being the total energy defined by, for an *ideal gas*,

$$\rho e = \rho C_v T + \frac{1}{2}\rho(u_1^2 + u_2^2 + u_3^2). \quad (2.3)$$

The fluxes F_i read, $\forall i \in \{1, 2, 3\}$,

$$\mathbf{F}_i = \begin{pmatrix} \rho u_i \\ \rho u_i u_1 - \sigma_{i1} \\ \rho u_i u_2 - \sigma_{i2} \\ \rho u_i u_3 - \sigma_{i3} \\ \rho e u_i - u_j \sigma_{ij} - k \frac{\partial T}{\partial x_i} \end{pmatrix}, \quad (2.4)$$

$k = \rho c_p \kappa$ being the thermal conductivity (and κ the thermal diffusivity).

The components σ_{ij} of the stress tensor are given by the Newton law

$$\sigma_{ij} = -p \delta_{ij} + \mu S_{ij}, \quad (2.5)$$

in which

$$S_{ij} = \left[\frac{\partial u_j}{\partial x_i} + \frac{\partial u_i}{\partial x_j} - \frac{2}{3}(\nabla \cdot \mathbf{u})\delta_{ij} \right] \quad (2.6)$$

denotes the deviatoric part of the strain-rate tensor. Bulk viscosity is neglected, as is commonly accepted, except in extreme thermodynamical situations. This yields

$$\mathbf{F}_i = \begin{pmatrix} \rho u_i \\ \rho u_i u_1 + p \delta_{i1} - \mu S_{i1} \\ \rho u_i u_2 + p \delta_{i2} - \mu S_{i2} \\ \rho u_i u_3 + p \delta_{i3} - \mu S_{i3} \\ (\rho e + p)u_i - \mu u_j S_{ij} - k \frac{\partial T}{\partial x_i} \end{pmatrix}. \quad (2.7)$$

Sutherland's empirical law

$$\mu(T) = \mu(273.15) \left(\frac{T}{273.15} \right)^{1/2} \frac{1 + S/273.15}{1 + S/T} \quad (2.8)$$

with

$$\mu(273.15) = 1.711 \times 10^{-5} \text{ Pl} \quad \text{and} \quad S = 110.4 \text{ K}$$

is prescribed for molecular viscosity, although the temperature variations are small in all the applications presented in this paper. Conductivity $k(T)$ is obtained assuming the Prandtl number $Pr = c_p \mu(T)/k(T)$ constant and equal to 0.7, as in air at ambient temperature. The equation of state

$$p = R \rho T \quad (2.9)$$

closes the system, with $R = C_p - C_v = \mathcal{R}/\mathcal{M} = 287.06 \text{ Jkg}^{-1}\text{K}^{-1}$ for air.

We omit here the details of the LES filtering procedure in the case of compressible turbulence, since compressibility effects are very low in our study. These details can be found in Ducros (1995) and Ducros *et al.* (1995). Basically, μ and k arising in (2.7) are replaced respectively by $\mu + \rho \nu_t$ and $k + \rho \nu_t c_p Pr_t^{-1}$, where the eddy viscosity ν_t will be specified below, and Pr_t is a turbulent Prandtl number taken equal to 0.6 as in isotropic turbulence. ρ now stands for the resolved density obtained by projection onto the computational grid; \mathbf{u} then denotes the resolved velocity field, associated to ρ in the sense of Favre averages (Favre 1965).

Now we present the FSF model as if the flow were of constant density. In the SF model (Métais & Lesieur 1992), it is assumed that the subgrid scales are close to isotropy and follow a Kolmogorov cascade. The cusp is also neglected. By subgrid energy conservation arguments,

$$\nu_t = \frac{2}{3} C_K^{-3/2} \left[\frac{E_x(k_C)}{k_C} \right]^{1/2} \quad (2.10)$$

is obtained, in which C_K is the Kolmogorov constant and $E_x(k_C)$ the local kinetic-energy spectrum at $k_C = \pi/\Delta$ of the resolved velocity field \mathbf{u} . This spectrum is determined in terms of the second-order structure function of \mathbf{u} , as if the turbulence were isotropic (Batchelor 1953):

$$F_2(\mathbf{x}, \Delta, t) = \langle \|\mathbf{u}(\mathbf{x} + \mathbf{r}, t) - \mathbf{u}(\mathbf{x}, t)\|^2 \rangle_{\|\mathbf{r}\|=\Delta} = 4 \int_0^{k_C} E_x(k, t) \left[1 - \frac{\sin k\Delta}{k\Delta} \right] dk. \quad (2.11)$$

In practice, $F_2(\mathbf{x}, \Delta, t)$ is computed over the six closest neighbours of point \mathbf{x} when the computational grid is uniform with cubic meshes. This is the *six-neighbour formulation*:

$$\begin{aligned} F_2(\mathbf{x}, \Delta, t) = \frac{1}{6} & \left[\|\mathbf{u}_{i+1,j,k} - \mathbf{u}_{i,j,k}\|^2 + \|\mathbf{u}_{i-1,j,k} - \mathbf{u}_{i,j,k}\|^2 \right. \\ & + \|\mathbf{u}_{i,j+1,k} - \mathbf{u}_{i,j,k}\|^2 + \|\mathbf{u}_{i,j-1,k} - \mathbf{u}_{i,j,k}\|^2 \\ & \left. + \|\mathbf{u}_{i,j,k+1} - \mathbf{u}_{i,j,k}\|^2 + \|\mathbf{u}_{i,j,k-1} - \mathbf{u}_{i,j,k}\|^2 \right]. \end{aligned} \quad (2.12)$$

For wall-bounded flows with meshes flattened in the direction x_2 normal to the wall, the *four-neighbour formulation* proposed by Normand & Lesieur (1992) is used. It reads

$$\begin{aligned} F_2(\mathbf{x}, \Delta, t) = \frac{1}{4} & \left[\|\mathbf{u}_{i+1,j,k} - \mathbf{u}_{i,j,k}\|^2 + \|\mathbf{u}_{i-1,j,k} - \mathbf{u}_{i,j,k}\|^2 \right. \\ & \left. + \|\mathbf{u}_{i,j,k+1} - \mathbf{u}_{i,j,k}\|^2 + \|\mathbf{u}_{i,j,k-1} - \mathbf{u}_{i,j,k}\|^2 \right]. \end{aligned} \quad (2.13)$$

The four-neighbour formulation is insensitive to velocity gradients normal to the wall, most of which come from the mean flow.

The expression for the SF model can be obtained very quickly by applying the mean-value theorem to (2.11): assuming E continuous, there exists a wavenumber $k_v \in [0, k_c]$ such that

$$E_x(k_v, t) = \frac{F_2(\mathbf{x}, \Delta, t)}{4 \int_0^{k_c} \left[1 - \frac{\sin k\Delta}{k\Delta}\right] dk} = \frac{\int_0^{k_c} E_x(k, t) \left[1 - \frac{\sin k\Delta}{k\Delta}\right] dk}{\int_0^{k_c} \left[1 - \frac{\sin k\Delta}{k\Delta}\right] dk}. \quad (2.14)$$

The value of k_v depends on the distribution of the resolved energy spectrum $E_x(k, t)$ over the whole span $[0, k_c]$; however, in the particular case of an infinite Kolmogorov cascade, one can replace $E_x(k, t)$ in (2.14) by $C_K \varepsilon^{2/3}(t) k^{-5/3}$ for all $k \in [0, k_c]$, yielding

$$k_v^{-5/3} = \frac{\int_0^{k_c} k^{-5/3} \left[1 - \frac{\sin k\Delta}{k\Delta}\right] dk}{\int_0^{k_c} \left[1 - \frac{\sin k\Delta}{k\Delta}\right] dk}. \quad (2.15)$$

Then (2.10) reads

$$v_t = \frac{2}{3} C_K^{-3/2} \left[\left(\frac{k_c}{k_v}\right)^{-5/3} \frac{F_2(\mathbf{x}, \Delta, t)}{4 \int_0^{k_c} \left[1 - \frac{\sin k\Delta}{k\Delta}\right] dk} \frac{1}{k_c} \right]^{1/2}, \quad (2.16)$$

from which k_v is eliminated thanks to (2.15), yielding the SF model

$$v_t(\mathbf{x}, t) = \frac{1}{3} C_K^{-3/2} \pi^{-4/3} \left[\underbrace{\int_0^\pi \xi^{-5/3} \left[1 - \frac{\sin \xi}{\xi}\right] d\xi}_{C_0} \right]^{-1/2} \Delta [F_2(\mathbf{x}, \Delta, t)]^{1/2} \\ \approx 0.105 C_K^{-3/2} \Delta [F_2(\mathbf{x}, \Delta, t)]^{1/2}, \quad (2.17)$$

since $C_0 \approx 0.478$.

In the filtered structure-function model, and in order to get rid of the large scales in the evaluation of v_t , we apply a high-pass filter to \mathbf{u} before computing its structure function. We chose a discrete Laplacian filter $HP^{(1)}$ iterated n times:

$$\tilde{\mathbf{u}}_{i,j,k}^{(n)} = HP^{(n)}(\mathbf{u}_{i,j,k}) \quad (2.18)$$

for $n \geq 1$, with

$$\tilde{\mathbf{u}}_{i,j,k}^{(1)} = HP^{(1)}(\mathbf{u}_{i,j,k}) = \mathbf{u}_{i+1,j,k} - 2\mathbf{u}_{i,j,k} + \mathbf{u}_{i-1,j,k} \\ + \mathbf{u}_{i,j+1,k} - 2\mathbf{u}_{i,j,k} + \mathbf{u}_{i,j-1,k} + \mathbf{u}_{i,j,k+1} - 2\mathbf{u}_{i,j,k} + \mathbf{u}_{i,j,k-1} \quad (2.19)$$

when the *six-neighbour* formulation (2.12) is used, and

$$\tilde{\mathbf{u}}_{i,j,k}^{(1)} = HP^{(1)}(\mathbf{u}_{i,j,k}) = \mathbf{u}_{i+1,j,k} - 2\mathbf{u}_{i,j,k} + \mathbf{u}_{i-1,j,k} + \mathbf{u}_{i,j,k+1} - 2\mathbf{u}_{i,j,k} + \mathbf{u}_{i,j,k-1} \quad (2.20)$$

when the *four-neighbour* formulation (2.13) is preferred.

Let $\tilde{E}_x^{(1)}$ be the spectrum of the field $\tilde{\mathbf{u}}^{(1)}$. It may be shown on some three-dimensional isotropic fields (white noise, Gaussian noise, developed isotropic turbulence, see Ducros 1995) that

$$\frac{\tilde{E}_x^{(1)}(k, t)}{E_x(k, t)} \approx 40 \left(\frac{k}{k_c} \right)^\beta, \quad (2.21)$$

with $\beta \approx 3.05$. It is different from the value $\beta = 4$ one should have for a true Laplacian, because of the finite differencing. Then, when the filter *HP* is applied n times, one obtains

$$\frac{\tilde{E}_x^{(n)}(k, t)}{E_x(k, t)} \approx 40^n \left(\frac{k}{k_c} \right)^{n\beta}. \quad (2.22)$$

When n is increased, the weight of the filter in the neighbourhood of k_c becomes more and more important, which is favourable for the purpose of eliminating the low-frequency oscillations. On the other hand, the boundary-layer simulations carried out with the filtered structure-function model developed below will blow up with $n > 3$. In this respect, the value $n = 3$ is the best choice. The Batchelor-type relationships (2.11) and (2.14) still hold when E_x and F_2 are replaced by their high-pass-filtered counterparts $\tilde{E}_x^{(n)}$ and $\tilde{F}_2^{(n)}$, respectively. Assuming, as in (2.15), a Kolmogorov cascade for $E(k, t)$ for all $k \in [0, k_c]$, one gets

$$k_v^{-5/3} \left(\frac{k_v}{k_c} \right)^{n\beta} = \frac{\int_0^{k_c} k^{-5/3} \left(\frac{k}{k_c} \right)^{n\beta} \left[1 - \frac{\sin k\Delta}{k\Delta} \right] dk}{\int_0^{k_c} \left[1 - \frac{\sin k\Delta}{k\Delta} \right] dk}. \quad (2.23)$$

$E_x(k_c)/k_c$ is now replaced by $(k_c/k_v)^{-5/3} \tilde{E}_x(k_v)/k_c = 40^{-n} (k_c/k_v)^{-5/3+n\beta} \tilde{E}_x^{(n)}(k_v)/k_c$ in (2.10), yielding

$$v_t(t) = \frac{2}{3} C_K^{-3/2} \left[40^{-n} \left(\frac{k_c}{k_v} \right)^{-5/3+n\beta} \frac{\tilde{F}_2^{(n)}(\mathbf{x}, \Delta, t)}{4 \int_0^{k_c} \left[1 - \frac{\sin k\Delta}{k\Delta} \right] dk} \frac{1}{k_c} \right]^{1/2}. \quad (2.24)$$

Elimination of k_v gives the following eddy viscosity for the FSF model:

$$v_t(\mathbf{x}, t) = \frac{1}{3} C_K^{-3/2} \pi^{-4/3} \left(\frac{\pi^\beta}{40} \right)^{n/2} \underbrace{\left[\int_0^\pi \xi^{-5/3+n\beta} \left[1 - \frac{\sin \xi}{\xi} \right] d\xi \right]}_{C_n}^{-1/2} \Delta \left[\tilde{F}_2^{(n)}(\mathbf{x}, \Delta, t) \right]^{1/2}. \quad (2.25)$$

For $n = 3$ and $\beta = 3.05$, $C_n \approx 1500$ and

$$v_t(\mathbf{x}, t) \approx 0.0014 C_K^{-3/2} \Delta \left[\tilde{F}_2^{(3)}(\mathbf{x}, \Delta, t) \right]^{1/2}. \quad (2.26)$$

We stress that in this formulation we have in fact evaluated the kinetic-energy spectrum $E_x(k_c)$ arising in equation (2.10) with the aid of a fictitious isotropic velocity field where large-scale fluctuations have been filtered out.

With this value of $n = 3$, the FSF model (FSF³) has worked successfully in the case of incompressible decaying isotropic turbulence at zero molecular viscosity (Comte

et al. 1994; Ducros 1995). Here, a pseudo-spectral (hence non-dissipative) code is used at a resolution of 64^3 , and the same kinetic-energy spectra are obtained as with the SF model. We recall that in this case the SF model gives energy spectra much closer to Kolmogorov's than Smagorinsky's model does (Métais & Lesieur 1992), and very close to the ones obtained with the dynamic model in the formulation by Ghosal *et al.* (1995). The FSF³ model, still at zero viscosity and with pseudo-spectral methods, turns out to be equivalent to the spectral-cusp eddy viscosity model, and less dissipative than the SF or Smagorinsky models for an incompressible temporal mixing layer forced quasi-two-dimensionally (see Silvestrini *et al.* 1995): the Kelvin–Helmholtz (KH) vortices are bigger, and the longitudinal hairpin vortices stretched in between are stronger. In the same paper, it is shown that, for a spatially growing mixing layer forced upstream quasi-two-dimensionally, the roll-up of KH vortices occurs about twice the distance downstream with the SF than with the FSF models. In this respect, the FSF model describes more properly the KH instability, which is inviscid and should not be affected by the subgrid model.

It has to be stressed that, like the SF model, the FSF model has no cusp from the Fourier point of view. It is only the kinetic-energy spectrum at k_C which is calculated in terms of a field where the large-scale fluctuations have been eliminated with a cusp-like filter. In this sense, there is no spectral backscatter in the FSF model. There is no backscatter in physical space either, since the eddy viscosity is always positive. However, it is well known from the works using the dynamic-modelling approach that negative eddy viscosities are not desirable in the sense that they yield computational instabilities. This is why the constants arising in the dynamic models have to be averaged in certain directions or planes in order to prevent these numerical problems. Another possible criticism of the FSF model is that it still relies upon the assumption of a Kolmogorov spectrum at the cutoff. At this point, we mention the model proposed by Lamballais, Lesieur & Métais (1996), where the spectral eddy viscosity (with a cusp) is corrected by a function of the kinetic-energy spectrum slope at k_C , derived from EDQNM non-local expansions (see Métais & Lesieur 1992). This 'dynamic spectral model' gives very good results for a turbulent channel, as far as the first- and second-order statistics are concerned, and should prove to be useful in the spatially growing boundary layer.

The superiority of the FSF model over the SF one for transitional flows is evident when looking at its asymptotic behaviour in the case of a discrete longitudinal sine wave $\tilde{\mathbf{u}}_{i,j,k} = U \cos(\omega i + \phi)$ of pulsation $\omega = k\Delta = \pi k/k_C$ and phase ϕ , in the long-wave limit $\omega \rightarrow 0$. For this signal, the second-order structure function given by (2.12) or (2.13) satisfies

$$F_2(\mathbf{x}, \Delta, t) = U^2 \left\{ [2 \sin^2 \phi] \omega^2 + [4i \cos \phi \sin \phi] \omega^3 + \left[\left(\frac{1}{2} \cos^2 \phi - \frac{2}{3} \sin^2 \phi \right) + 2i^2 (\cos^2 \phi - \sin^2 \phi) \right] \omega^4 + O(\omega^5) \right\}, \quad (2.27)$$

i.e. scales in general on ω^2 . The eddy viscosity given by the SF model then scales on ω . On the other hand,

$$\tilde{F}_2^{(n)} = [2(\cos \omega - 1)]^n F_2, \quad (2.28)$$

which gives a scaling in ω^{2n+1} for the FSF model.

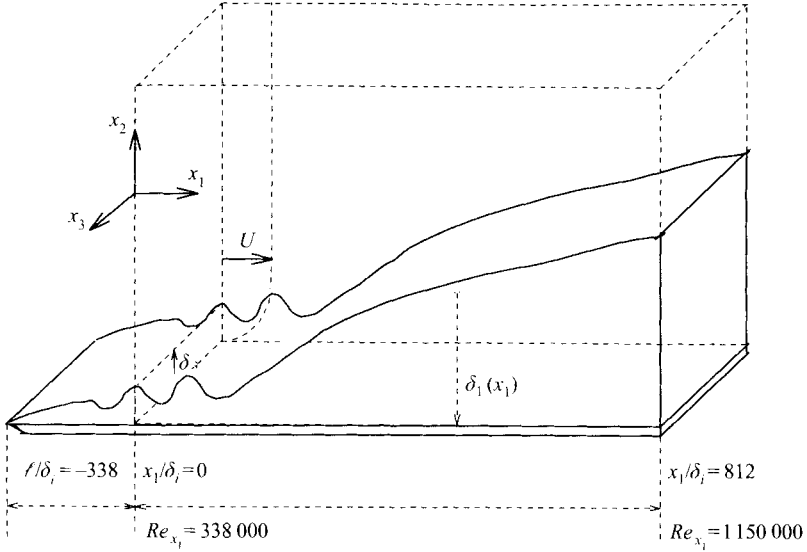


FIGURE 1. Spatially developing boundary layer over a flat plate; the computational domain extends between 0 and $812\delta_i$ (after Guo *et al.* 1995).

3. Calculation procedure

We present the large-eddy simulation of a forced boundary layer at $M_\infty = 0.5$, developing spatially in the laboratory frame. We thus have $p_\infty = 1/(\gamma M^2)\rho_\infty U_\infty^2 \approx 5.7(\frac{1}{2}\rho_\infty U_\infty^2)$ and the external temperature is $T_\infty = 273$ K. The FSF³ model is used in its four-points formulation (2.13), (2.18) and (2.20).

Let x_1 , x_2 and x_3 denote the streamwise, transverse and spanwise directions respectively. The calculation box has the following dimensions: $L_1 = 812\delta_i$, $L_2 = 2\delta_i$, $L_3 = 22\delta_i$, in which $\delta_i = \delta_1(x_1 = 0)$ denotes the upstream displacement thickness. The numbers of grid points in each direction are $N_1 = 650$, $N_2 = 32$ and $N_3 = 20$, respectively (see figure 1, after Guo, Adams & Kleiser 1995).

The upstream Reynolds number based on δ_i is $Re_{\delta_i} = 1000$. Assuming a Blasius spreading law from a fictitious leading edge at abscissa ℓ (negative) and the upstream boundary $x_1 = 0$, one has (see e.g. Schlichting 1987)

$$\delta(x_1) = 1.721 \left[\frac{v(x_1 - \ell)}{U_\infty} \right]^{1/2}, \quad (3.1)$$

which yields $\ell = -338\delta_i$, hence $Re_{x_1} = [(x_1 - \ell)/\delta_i] Re_{\delta_i} \in [3.4 \times 10^5, 1.15 \times 10^6]$ for $x_1 \in [0, L_1]$. This should permit observation of the complete transition.

The simulation is carried out using the code described in Normand & Lesieur (1992). The grid, uniform in the streamwise and spanwise directions, is stretched in the direction normal to the wall, the height of each grid point being given by

$$x_2(j) = L_2 \frac{C \eta}{1 + C - \eta}, \quad \eta = \frac{j-1}{N_2-1}. \quad (3.2)$$

The constant C controls the stretching ($C = 0.03$ in our case). The mesh line $j = 2$ lies at $x_2 = 0.13\delta_i$, which corresponds to $x_2^+ = 4.7$, with a friction velocity $u_\tau = 0.038U_\infty$ typical of the turbulent region in our simulation (see the next section). In the same way, $\Delta x_1 = 1.25\delta_i$ and $\Delta x_3 = 1.16\delta_i$ correspond to $\Delta x_1^+ = 44$ and $\Delta x_3^+ = 41$,

respectively. This can be compared with the resolution $(\Delta x_1^+, \Delta x_3^+) = (80, 14)$, and $x_2^+ \approx 1$ for the first point near the wall, chosen by Yang & Voke (1993) for their LES of by-pass transition and $(\Delta x_1^+, \Delta x_3^+) = (28, 10)$, chosen by Rai & Moin (1993) for their DNS.

By comparison with the resolution required for DNS in the temporal case $(\Delta x_1^+, \Delta x_3^+) = (20, 6.7)$ and $x_2^+ \approx 1$ for the first point near the wall (Spalart 1988), our resolution near the wall is too low to expect a good description of the viscous sublayer in the turbulent regime. This will be at the origin of a decrease of the velocity gradient at the wall, and hence of the friction velocity, with respect to measurements.

At the wall, we prescribe a no-slip condition for the velocity ($\mathbf{u} = 0$) and an adiabatic condition for the temperature: $(\partial T / \partial x_2)_{x_2=0} = 0$. We assume periodicity in the spanwise direction and adopt non-reflective boundary conditions prescribed through the Thompson characteristic method for the outflow and the upper boundary layer (Thompson 1987).

The upstream boundary condition is given by

$$U(0, x_2, x_3, t) = U_{lam}(x_2) + 5 \times 10^{-3} \hat{U}(x_2) + 8 \times 10^{-3} U_{rand}(x_2, x_3, t), \quad (3.3)$$

where $U_{lam}(x_2)$ is the laminar solution of the similarity equations, $\hat{U}(x_2)$ is the most amplified eigenmode of two-dimensional Tollmien–Schlichting (TS) waves (wavelength $\lambda_{TS} = 21\delta_i$), and $U_{rand}(x_2, x_3, t)$ is a randomly chosen three-dimensional white noise of variance U_∞^2 . The amplitude of the two-dimensional forcing is relatively low, just high enough to trigger the secondary instabilities which develop on the TS waves: Spalart & Yang (1987) did not observe transition through secondary instability for amplitudes of TS waves below $4 \times 10^{-3} U_\infty$. The level of three-dimensional forcing is of the same order as residual turbulence for in-flight conditions.

At $t = 0$, we impose a two-dimensional Blasius-like profile resulting from the resolution of the similarity equations. We perform the three-dimensional simulation during a period $2.25T_A$, where $T_A = 2320\delta_i/U_\infty$ is the time required to travel downstream through the computational domain at the propagation speed $c = 0.35U_\infty$ of the waves we observe (see the discussion in §4.3). This is long enough to reach the steady regime. Time sampling is then performed for a short period, $T_A/10$. The whole operation requires about 80 hours of CPU time on a CRAY 2, which is about 10 times less than the DNS of Rai & Moin (1993).

All the visualizations presented here are taken at the final time-step of the calculation (after time sampling). In some of them (figures 13–16, 18, 19, 22–24, 28–30), the domain is duplicated in the spanwise direction owing to periodicity, in order to give a better idea of the flow topology. In fact, our calculation domain is very narrow, since its spanwise extent is of the order of one upstream TS wave. In this respect, it may be considered as a minimal spatial boundary layer, in the same sense as the ‘minimal channel’ simulated by Jimenez & Moin (1991).

4. Results

4.1. Quality check

The streamwise evolutions of the time- and-spanwise-averaged

- displacement thickness $\langle \delta_1 \rangle(x_1)$,
- momentum thickness $\langle \delta_2 \rangle(x_1)$,

shape factor $H_{12}(x_1) = \langle \delta_1 \rangle(x_1) / \langle \delta_2 \rangle(x_1)$,
skin-friction coefficient

$$C_f(x_1) = \frac{1}{\frac{1}{2}\rho_\infty U_\infty^2} \left[\mu[\langle T \rangle(x_1, x_2)] \frac{\partial[\langle u_1 \rangle(x_1, x_2)]}{\partial x_2} \right]_{x_2=0} = 2 \left[\frac{u_\tau(x_1)}{U_\infty} \right]^2 \quad (4.1)$$

are shown figure 2, together with (in dashed lines) the following laminar and turbulent empirical laws, found in Cousteix (1989):

$$\delta_{1_{lam}}(x_1) = 1.721 Re_{\delta_i}^{-1/2} \left(\frac{x_1 - \ell'}{\delta_i} \right)^{1/2}, \quad (4.2a)$$

$$\delta_{2_{lam}}(x_1) = 0.664 Re_{\delta_i}^{-1/2} \left(\frac{x_1 - \ell'}{\delta_i} \right)^{1/2}, \quad (4.2b)$$

$$C_{f_{lam}}(x_1) = 0.664 Re_{\delta_i}^{-1/2} \left(\frac{x_1 - \ell'}{\delta_i} \right)^{-1/2}, \quad (4.2c)$$

and

$$\delta_{1_{tur}}(x_1) = 0.0309 Re_{\delta_i}^{-1/6} \left(\frac{x_1 - \ell'}{\delta_i} \right)^{5/6}, \quad (4.3a)$$

$$\delta_{2_{tur}}(x_1) = 0.0221 Re_{\delta_i}^{-1/6} \left(\frac{x_1 - \ell'}{\delta_i} \right)^{5/6}, \quad (4.3b)$$

$$C_{f_{tur}}(x_1) = 0.0368 Re_{\delta_i}^{-1/6} \left(\frac{x_1 - \ell'}{\delta_i} \right)^{-1/6}. \quad (4.3c)$$

In (4.3), self-similar turbulent spreading is assumed immediately from a virtual leading edge at abscissa ℓ' . From figures 2(a, b), the best fit is $\ell' = 125\delta_i$, which makes our C_f under-estimated by 25%. Consequently, our turbulent velocity profiles depart somewhat from the expected law of the wall, especially in the logarithmic region (figure 3). Note that a similar trend is observed, to a much lesser extent, in the DNS of Rai & Moin (1993).

On the optimistic side, the exponents 5/6 and $-1/6$ are not too badly estimated between $x_1 = 470\delta_i$ and, at least, $650\delta_i$, i.e. $Re_{x_1} \in [0.88 \times 10^6, 0.99 \times 10^6]$; the laminar laws are correctly recovered, which is a good point for the FSF³ model. The shape of the curves during the transition conforms to expectations (in particular the dip of $\langle \delta_1 \rangle$, but not of $\langle \delta_2 \rangle$, see e.g. Cousteix 1989, p. 298). The shape factor decreases from the Blasius value of 2.6 down to 1.5, which is slightly larger than the expected value $0.0309/0.0221 = 1.4$. In fact, this value depends on the Reynolds number after transition, which is $Re_{\delta_i} \approx 1900$ in our case. For $Re_{\delta_i} \approx 2000$, Murlis, Tsai & Bradshaw (1982) and Spalart (1988) report 1.45 and 1.43, respectively.

From figure 2(c), one can work out a ‘transition point’ at $x_1 \approx 250\delta_i$ and hence a ‘transition Reynolds number’ $Re_{x_1} \approx 0.59 \times 10^6$. In natural transition, this value would be obtained for a level of free-stream turbulence of intensity of 1% (experiments of Hall & Hislop 1938, see the review in Schlichting 1987), probably through a different scenario of transition.

4.2. Streaks

In order to help the interpretation of the visualizations that follow, the instantaneous extrema of vorticity, velocity and pressure are plotted as a function of x_1 , in figures 4, 5 and 6, respectively. The solid lines correspond to values recorded at the wall,

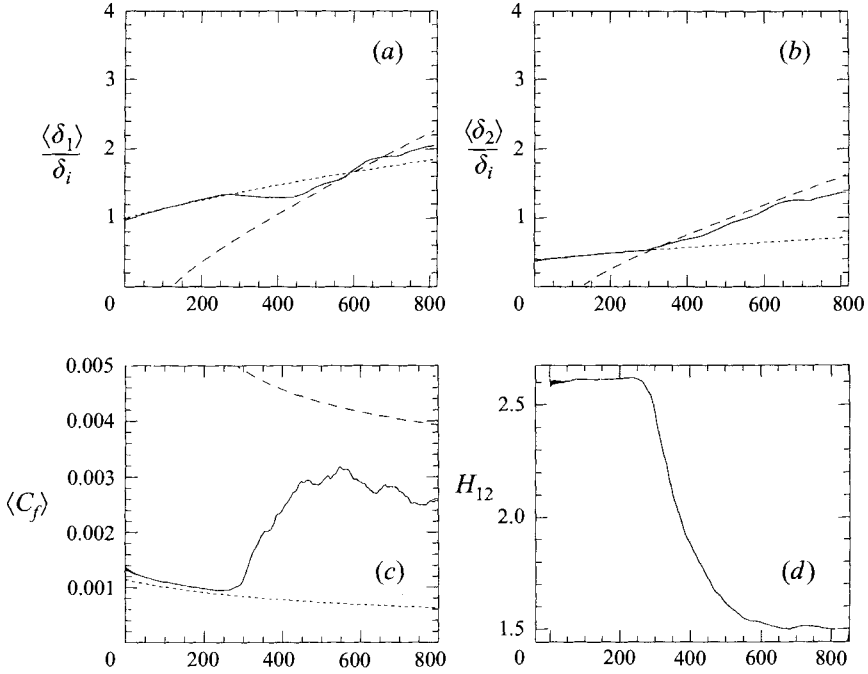


FIGURE 2. Streamwise evolution of the time- and spanwise-averaged displacement and momentum thicknesses, skin-friction coefficient and shape factor (*a*, *b*, *c* and *d*, respectively). The dotted lines correspond to the empirical laws (4.2), and the dashed ones to their turbulent counterparts (4.3) with $\ell' = 125\delta_i$.

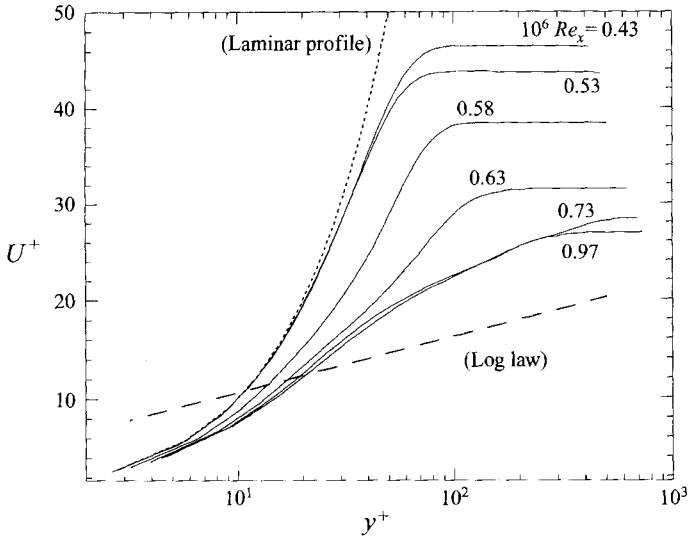


FIGURE 3. Time- and spanwise-averaged velocity profile $U^+ = \langle u_1 \rangle / u_\tau$ as a function of $x_2^+ = \rho_\infty u_i x_2 / \mu = (\frac{1}{2} C_f)^{1/2} Re_{\delta_i, x_2} / \delta_i$ for six streamwise positions, together with the usual laws of the wall, $U^+ = x_2^+$ and $U^+ = \ln x_2^+ / 0.41 + 5$. Our profiles no longer evolve from $Re_x = 0.77 \times 10^6$ onwards.

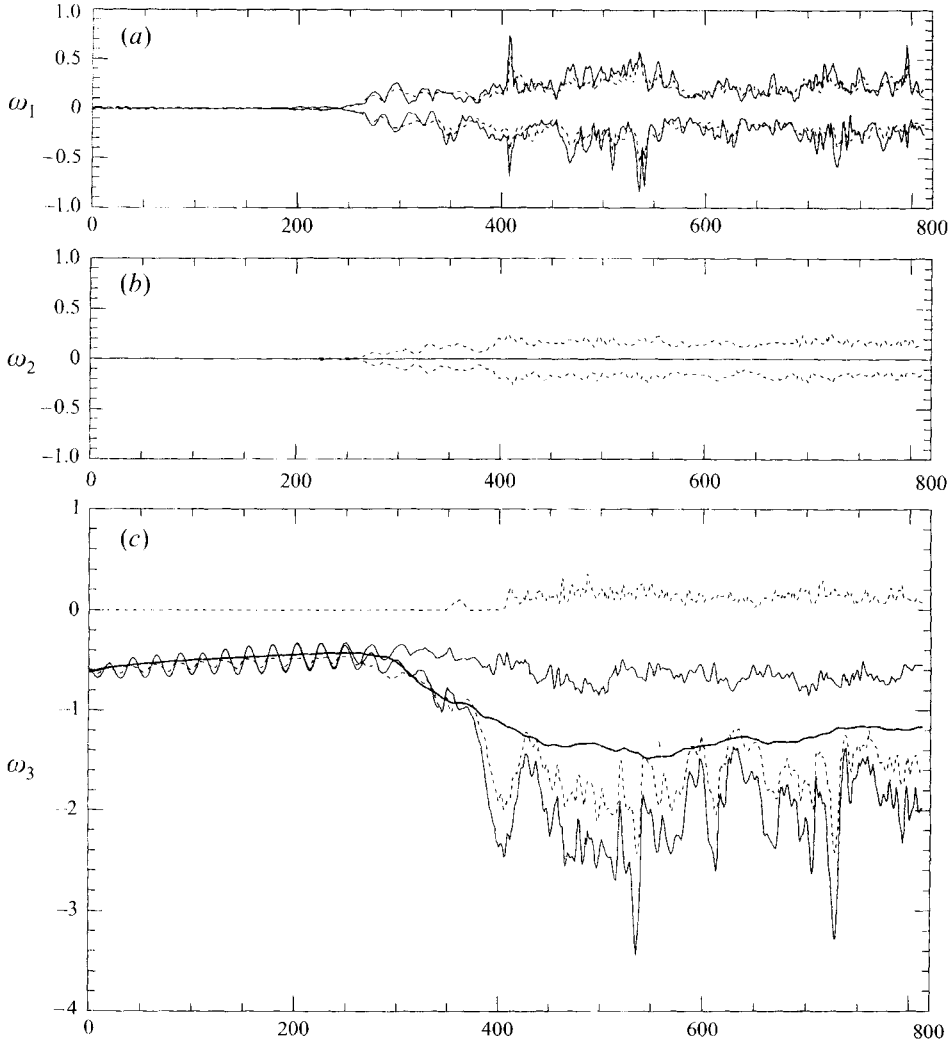


FIGURE 4. Streamwise evolution of the extrema of vorticity at given x_1 . The axes are normalized by δ_i horizontally and U_∞/δ_i vertically: (—) and instantaneous min and max values at the wall (\cdots), away from the wall. The thick line in (c) is the time- and spanwise-averaged ω_3 at the wall.

the dashed lines to interior points. The streamwise vorticity component (figure 4a) remains close to zero up to transition. Downstream, the minima and maxima of ω_1 oscillate in a fairly symmetrical fashion, between $-0.8U_\infty/\delta_i$ and $0.8U_\infty/\delta_i$. These extrema are very localized, and are reached at the wall. In contrast, the ‘vertical’ vorticity component ω_2 , which is necessarily zero at the wall, behaves more calmly with a quasi-uniform distribution of extrema at $\approx \pm 0.2U_\infty/\delta_i$. The heavy solid line in figure 4(c) is the time- and spanwise-averaged spanwise vorticity at the wall $\langle \omega_3 \rangle_w(x_1) = -[\partial \langle u_1 \rangle / \partial x_2]_w = -(\rho_\infty / \mu_w) u_\tau^2$ (i.e. figure 2c again, from a different point of view). In the laminar regime, $\langle \omega_3 \rangle_w(x_1)$ and u_τ are of the order of $-0.5U_\infty/\delta_i$ and $0.025U_\infty$, respectively. After transition, they become $\approx -1.5U_\infty/\delta_i$ and $0.038U_\infty$, respectively. At the wall, the lowest values of ω_3 are $\approx -3.5U_\infty/\delta_i$, which corresponds to shear more than twice as large as its mean value. These minima are correlated with the extrema of ω_1 mentioned above. More regular is the distribution of the maxima

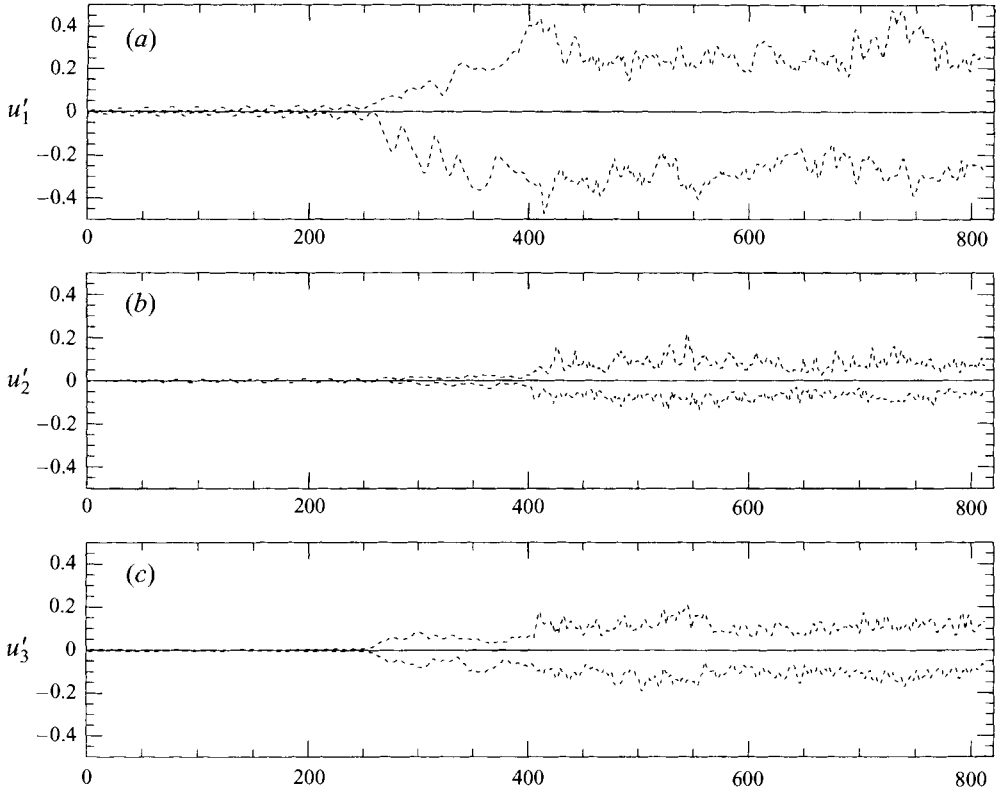


FIGURE 5. Same as figure 4 but for the instantaneous extrema of velocity fluctuations (normalized by U_∞). The extrema of u_2 are the same as those of u'_2 .

of ω_3 at the wall, their typical value being close to $-0.5U_\infty/\delta_i$, which is reminiscent of the laminar regime. It is tempting to associate these maxima with *low-speed streaks*, as defined in Klebanoff, Tidstrom & Sargent (1962) as the result of *peak-and-valley splitting* of the whole turbulent flow. Since these maxima are $\approx U_\infty/\delta_i$ above the mean, we *a priori* expect *high-speed streaks* in which the minimal values of ω_3 would be about U_∞/δ_i below the mean, i.e. between $\approx -2.5U_\infty/\delta_i$. In figure 4(c), this corresponds to an average value of the minima, but not to the peaks at $-3.5U_\infty/\delta_i$ mentioned above, which are also associated with peaks of streamwise vorticity. These intermittent peaks are then likely to correspond to violent vortical events occurring within high-speed streaks. They are associated with peaks of streamwise velocity fluctuations (figure 5a) at about $\pm 0.5U_\infty$, the average value of the extrema of u'_1 being half the size, with a symmetrical repartition between positive and negative values (except maybe between $250\delta_i$ and $400\delta_i$ where the curve of the minima oscillates more than that of the maxima). The 'vertical' velocity fluctuations u'_2 remain small up to $\approx 400\delta_i$. From there, they rapidly reach $\pm 0.1U_\infty$, with peaks at $+0.2U_\infty$ apparently related to the violent events mentioned above. This is somewhat surprising because the vertical velocity fluctuations are expected to be negative in the high-speed streaks. We will come back to this point later.

The extrema of spanwise velocity fluctuations (figure 5c) start taking off as from $x_1 = 250\delta_i$, where they level off at $\pm 0.1U_\infty$, with an episode at $\pm 0.2U_\infty$ between $400\delta_i$ and $550\delta_i$. From the inlet to $\approx 300\delta_i$, the pressure extrema (figure 6) oscillate at

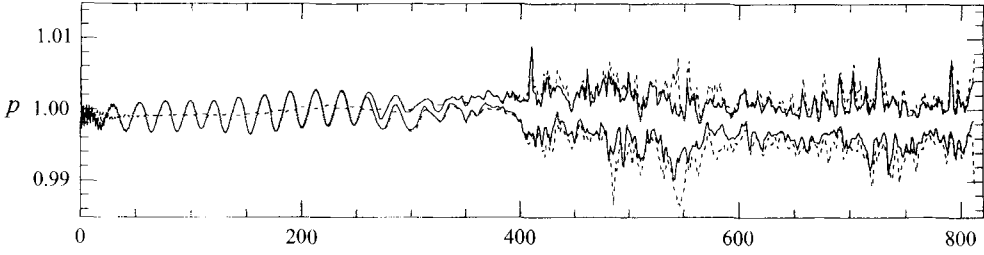


FIGURE 6. Streamwise evolution of the extrema of pressure, normalized by $p_\infty = (1/\gamma M^2)\rho_\infty U_\infty^2 \approx 5.7(\frac{1}{2}\rho_x U_x^2)$ at given x_1/δ_i , at the wall (solid line) and away from the wall (dotted lines).

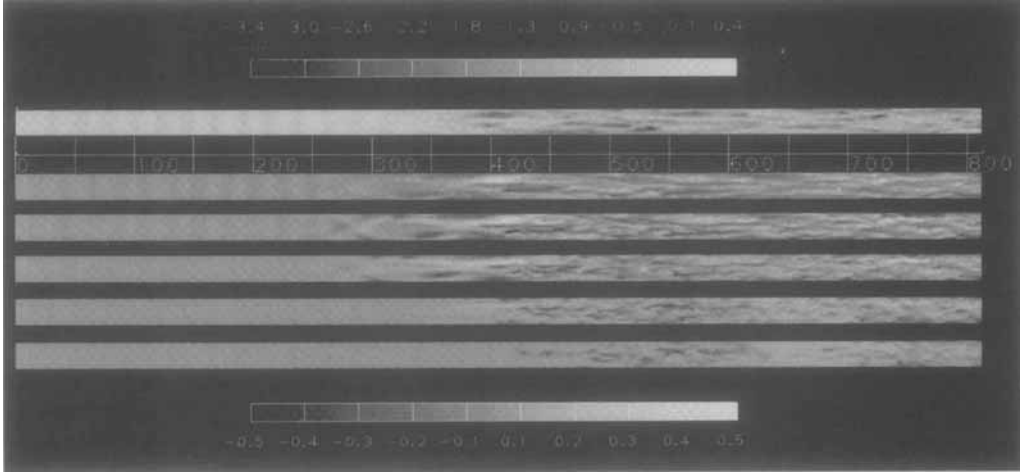


FIGURE 7. From top to bottom: map of ω_3 at the wall, and five slices of u'_j at the following heights (the rightmost column assumes $u_t = 0.038U_x$, which is an average value over the region $x_1/\delta_i \in [470, 650]$).

j	x_2/δ_i	x_2^4
4	0.42	15
8	1.10	39
12	1.98	71
17	3.52	127
22	5.92	216

approximately constant amplitude and wavelength, the latter being that of the TS waves injected, i.e. $21\delta_i$. At the wall, the curves of minimal and maximal pressure (solid lines) collapse, showing that these waves remain two-dimensional as they propagate. This is also true away from the wall, the amplitude of the oscillations decreasing as the distance to the wall increases. Between $\approx 300\delta_i$ and $400\delta_i$, i.e. where most of the changes in the mean velocity profile occur (see figure 2d), the pressure fluctuations practically vanish. It is only from $400\delta_i$ that the pressure extrema exhibit a turbulent behaviour, with an average amplitude of about $\pm 2 \times 10^{-3} p_x$, i.e. $\approx \pm 10^{-2}(\frac{1}{2}\rho_x U_x^2)$, and peaks at $\pm 10^{-2} p_x$, i.e. $\approx \pm 6 \cdot 10^{-2}(\frac{1}{2}\rho_x U_x^2)$, which is rather small in comparison with the values recorded in free-shear flows like mixing layers and jets. In contrast to isotropic turbulence or free-shear flows, the high-pressure fluctuations are as large as the low-pressure ones. Note that the event at $410\delta_i$ mentioned above (that might not deserve the epithet ‘violent’ after all) corresponds to a peak of high pressure at the

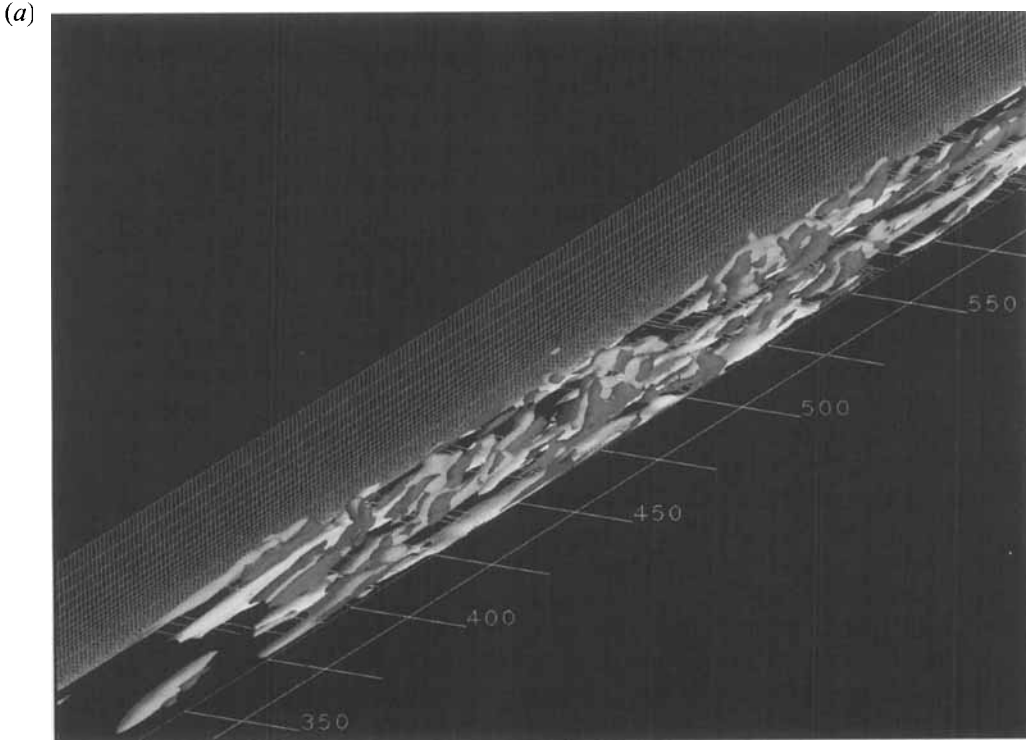


FIGURE 8. (a) Transitional region: vortex lines and isosurfaces (same thresholds as for (b)). (b) Turbulent region: isosurfaces $\omega_3 = -1.2U_\infty/\delta_i$ (white) $\omega_2 = 0.12U_\infty/\delta_i$ (red), $\omega_2 = -0.12U_\infty/\delta_i$ (blue), $u'_1 = 0.20U_\infty$ (yellow) and $u'_1 = -0.20U_\infty$ (green); vortex lines originating from 80 points, randomly selected, where $-\omega_3$ is larger than U_∞/δ_i .

wall, the other peaks being preferentially reached away from the wall. It therefore seems that this first peak at the wall is of importance, and that it plays a role in the transition process.

Contour maps of skin friction coefficient and streamwise velocity fluctuations like figure 7 can be criticized for being too dependent on the choice of the colourmaps. They are nevertheless good at giving a general overview of the flow. In particular, they confirm the clear-cut character of the three regions identified above:

(i) from the inlet to $x_1 \approx 250\delta_i$, we can see the two-dimensional signature of the TS waves we use for the forcing. One can check visually that their amplitude and period hardly change as they propagate downstream.

FIGURE 9. Contour maps of u'_1 at $i = 332$ (i.e. $x_1 = 414\delta_i$ and $Re_x = 0.75 \times 10^6$) on the left, and at $i = 582$ (i.e. $x_1 = 727\delta_i$ and $Re_x = 1.11 \times 10^6$) on the right. The positive values are in purple, the negative in yellow.

FIGURE 17. Slice of ω'_1 with a colourmap which emphasizes the small variations around the mean. The white and dark isosurfaces correspond to $p = 1.001p_\infty$ and $0.999p_\infty$, respectively, that is, $p_\infty \pm 0.002$ ($\frac{1}{2}\rho_\infty U_\infty^2$). In order to make them more visible, the whole view is tilted by 1° around the x_2 axis. Note that, because of the slice, only the portion $x_3/\delta_i \in [20, 22]$ of the domain is visible, which masks the growing three-dimensionality of the isosurfaces.

(b)

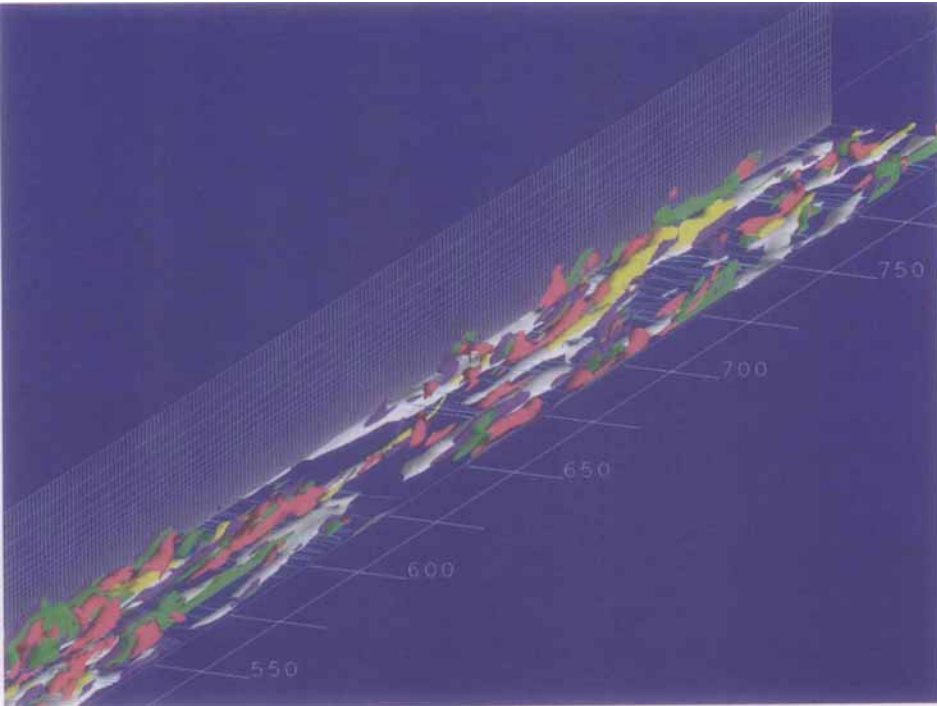


FIGURE 8(b). For caption see facing page.

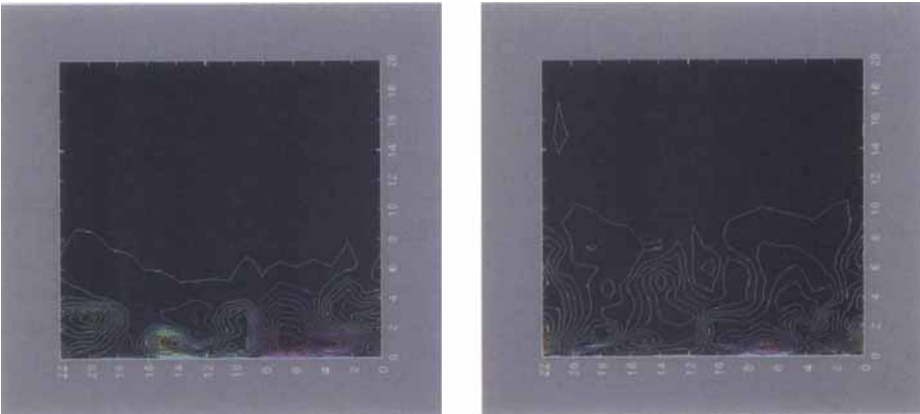


FIGURE 9. For caption see facing page

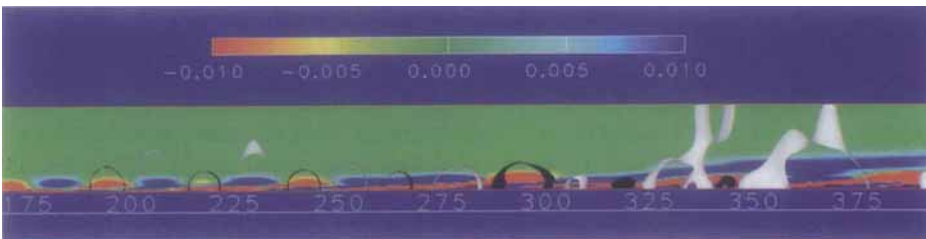


FIGURE 17. For caption see facing page

(ii) From $x_1 \approx 250\delta_i$ to $400\delta_i$, i.e. $Re_{x_1} \approx 0.74 \times 10^6$, oblique waves emerge in a staggered pattern, followed by a streamwise instability giving rise to streaks. This will be discussed below, in §4.3. Note that $\langle \delta_1 \rangle(x_1)$ keeps decreasing in this region.

(iii) From $x_1 \approx 400\delta_i$ onwards, the streaks rapidly become turbulent, but keep a strong streamwise coherence which might be forced by our domain being narrow. Indeed, figures 7 and 8 show structures stretching longitudinally over $100\delta_i$, i.e. 3800 wall units, with the value $u_\tau = 0.038U_\infty$ typical of the region $x_1/\delta_i \in [470, 650]$. The length of the streaks in wide boundary layers or plane channels is $\simeq 1000$ wall units. In the same vein, because of our low resolution, the spanwise ‘period’ of the streak system is widely over-estimated: we have, on average, two periods of streaks within the span. Our streak spacing is thus of the order of $11\delta_i$, i.e. about 400 wall units, which is four times the commonly accepted value.

Figure 7 also confirms that drag (i.e. $|\omega_3|$ at the wall) is large below the high-speed streaks, and close to its laminar value below the low-speed streaks. More precisely, figure 8(a, b) shows that the regions of high drag literally creep at the wall (the thickness of the white isosurface $\omega_3 = -1.2U_\infty/\delta_i$ is never larger than 15 wall units). The vortex lines which pass through them (in light blue) are oriented spanwise, without much three-dimensionality even in the turbulent portion of the domain. They wiggle in phase, which indicates the presence of a purely spanwise (i.e. independent of time) unstable mode. Although our resolution at the wall is too low to be conclusive, there do not seem to be any streamwise vortex tubes in the near-wall region. In contrast, the vortex lines located higher up, not shown here, carry less vorticity but tend to form hairpins.

In order to give an idea of the vertical extent of the streak system, figure 8 also shows the isosurfaces $u'_1 = \pm 0.2U_\infty$ (high-speed in yellow, low-speed in green) and that of vertical vorticity $\omega_2 = \pm 0.12U_\infty/\delta_i$ (positive in red, negative in blue). These thresholds correspond to the average values of the extrema plotted in figures 5 and 4. The respective arrangement of these isosurfaces conforms to the model of *peak-and-valley splitting* introduced by Klebanoff *et al.* (1962). In particular, vertical vorticity is created between the high-speed and the low-speed streaks, which explains the flat vertical shape of the red and blue isosurfaces which surround the high-drag regions. Their height is approximately the same as that of the u'_1 isosurfaces: ≈ 200 wall units, which is larger than the average vorticity thickness of the layer. We therefore can say that the peak-and-valley splitting practically concerns the whole of the boundary layer. However, cross-sections of the u'_1 field (in particular figure 9a, b) shows concentrations of u'_1 lying between 10 and 55 wall units away from the wall, i.e. in the buffer region.

Figure 9(a, b) is taken where u'_1 reaches its extrema, and the corresponding local instantaneous profiles are plotted in figure 10, showing points of inflection in the low-speed streaks (solid line with stars), both in the transitional and the turbulent regimes ((a) and (b) respectively). Plotted in wall units using time- and spanwise-averaged values of u_τ , these profiles collapse in the outer region but strongly differ close to the wall (figure 11). In particular, we find again from figures 10(b) and 11(b) that the average wall shear stress is under-estimated, since the low-speed profiles are closer to the average profiles (shaded triangles) than the high-speed ones (hollow triangles). This shows up again when these profiles are redrawn using local instantaneous values of u_τ (figure 12) instead of its average value, in order to make them collapse close to the wall: in contrast with the high-speed profile, the low-speed profile in the part (b) does not change much, because its local u_τ is close to the average.

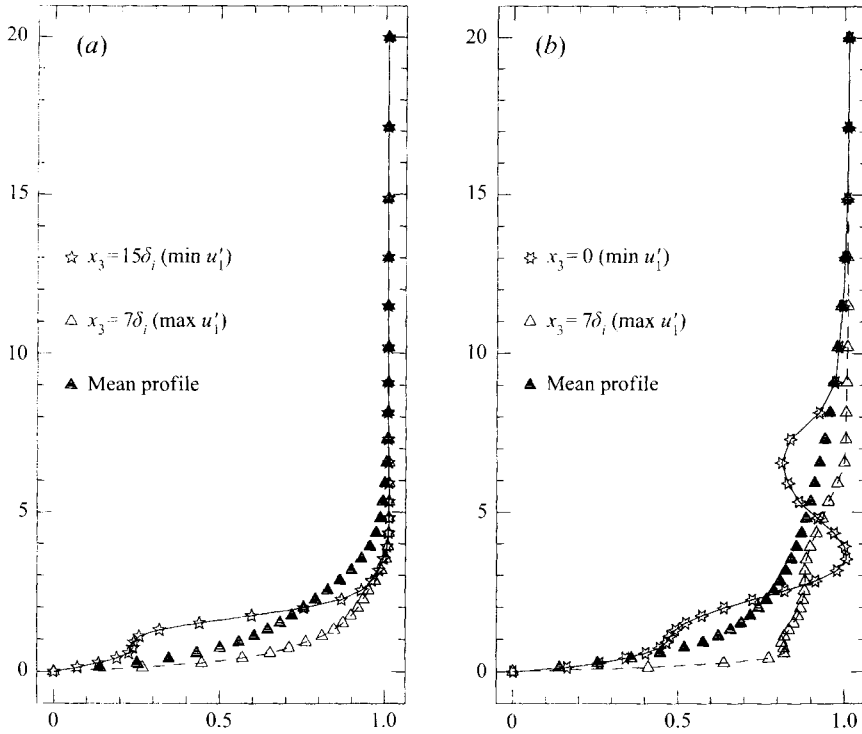


FIGURE 10. (a) Local instantaneous velocity profiles at $x_1 = 414\delta_i$ (or $Re_{x_1} = 0.75 \times 10^6$), where u'_1 reaches its minimum, $\text{Min}U'_1$. The local maximum at the same abscissa is denoted $\text{max}U'_1$. (b) As (a) but same at $x_1 = 728\delta_i$ (or $Re_{x_1} = 1.07 \times 10^6$), where u'_1 reaches its maximum.

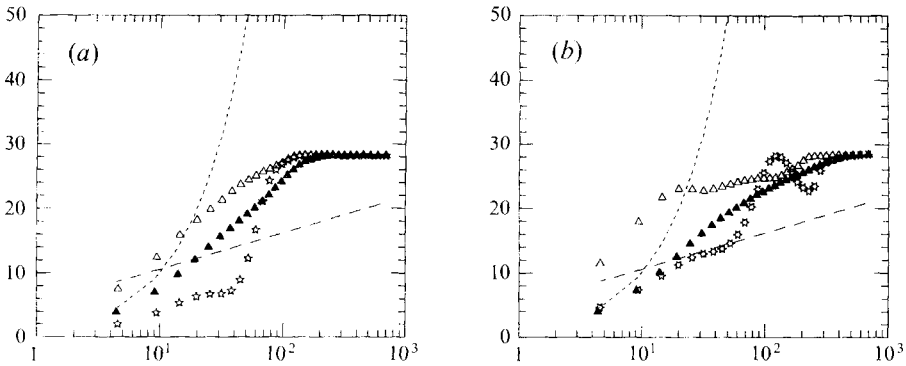


FIGURE 11. Same as figure 10, in wall coordinates, using time- and spanwise-averaged values of u_τ . The dotted and dashed lines correspond to the laws of the wall $U^+ = x_2^+$ and $U^+ = \ln x_2^+ / 0.41 + 5$ respectively, as in figure 3.

When the levels of the u'_1 isosurfaces are reduced by a factor $\simeq 10$ (figure 13), ‘laminar-looking’ streaks become visible between about $320\delta_i$ and $400\delta_i$, that is, $Re_x \in [0.66 \times 10^6, 0.74 \times 10^6]$. Note that this interval corresponds to the transition region, where the velocity profile changes from laminar to turbulent. These streaks start looking turbulent from the high-pressure event at $x_1 = 410\delta_i$ mentioned earlier. Calculations at higher resolution will be performed soon in order to clarify what is

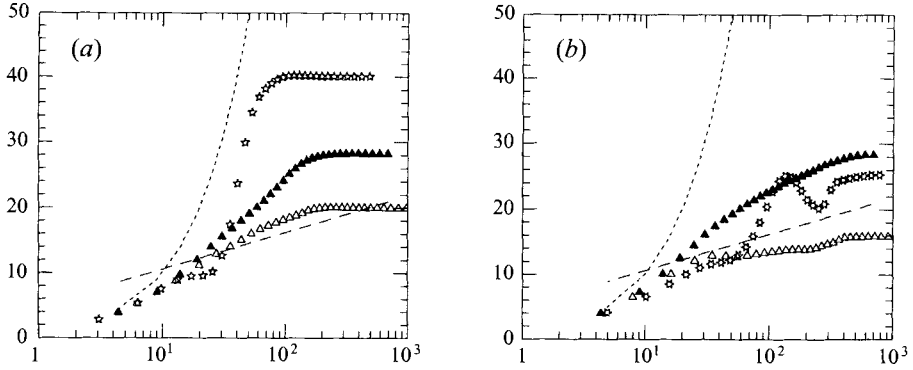


FIGURE 12. Same as figure 11, but using the local instantaneous values of u_t .

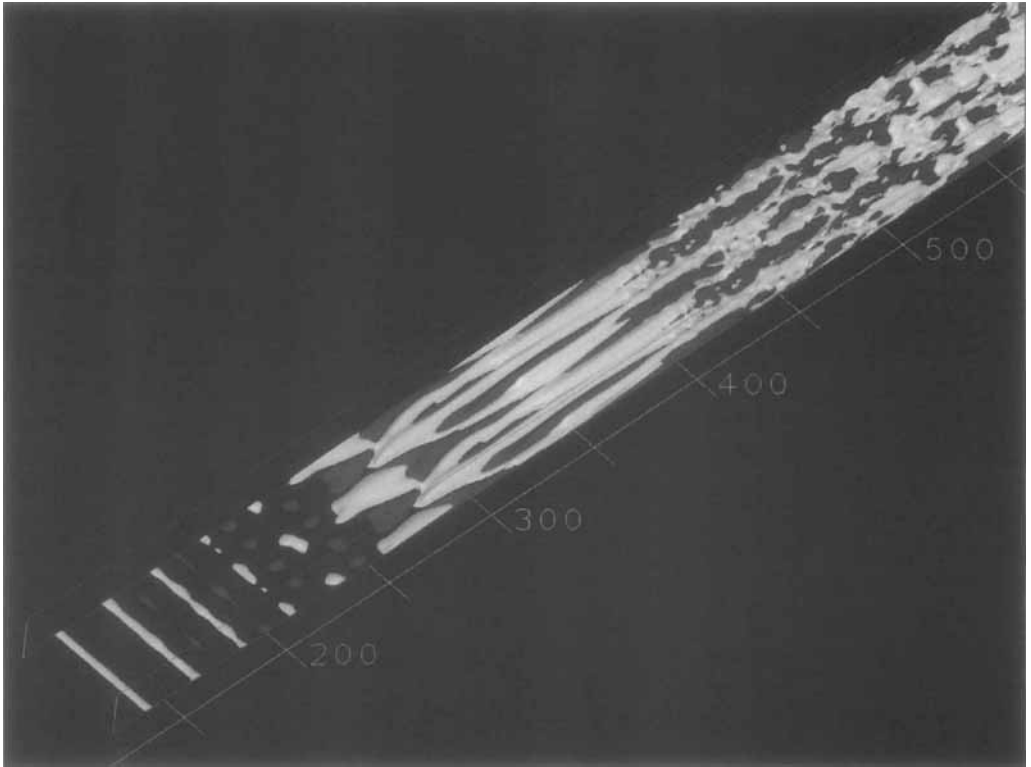


FIGURE 13. Isosurfaces $u'_1 = 0.024U_\infty$ (white) and $u'_1 = -0.024U_\infty$ (dark). The domain has been duplicated in the spanwise direction.

going on there. For the moment, all we can say is that this event (which appears as a white spot of large positive u'_1 in figure 7) coincides with a region where a 'laminar-looking' high-speed streak (in white in figure 13) pitchforks, yielding a 'turbulent-looking' low-speed streak (in dark) flanked by two 'turbulent-looking' high-speed streaks. It therefore seems reasonable to conjecture the presence of a stagnation point at the wall, which would account for the high-pressure peak observed in figure 6. On

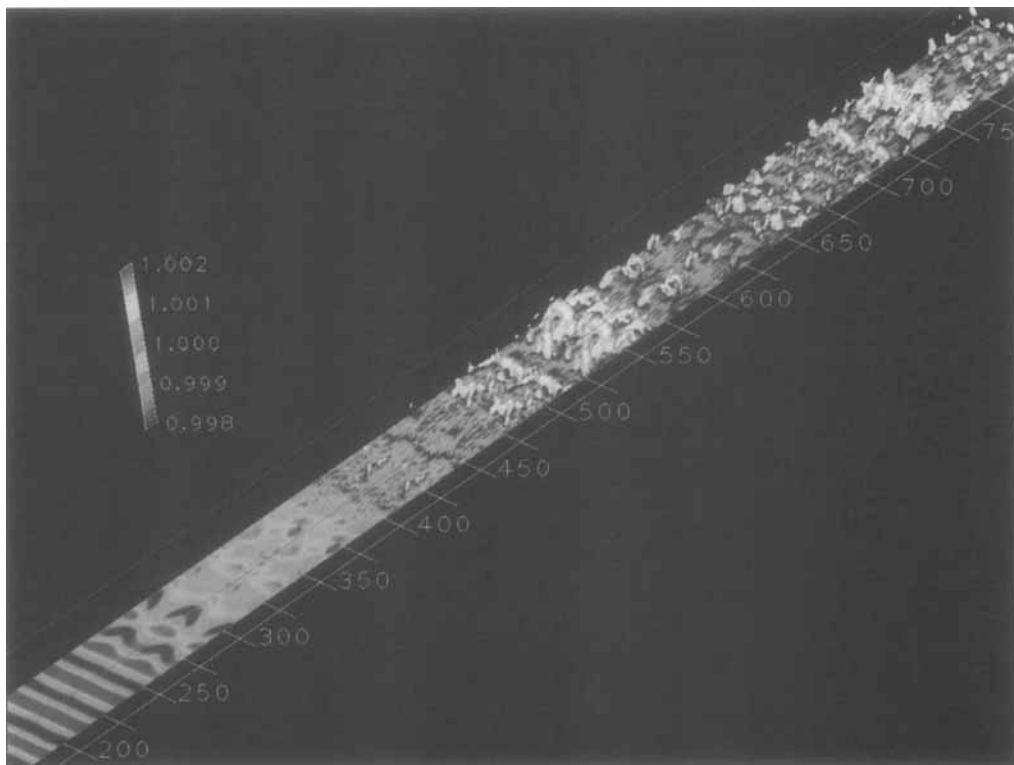


FIGURE 14. Map of the wall pressure, with a colour map which emphasizes the small variations around the mean. The white isosurface corresponds to a lower value: $0.996 p_\infty \approx p_\infty - 0.023 (\frac{1}{2} \rho_\infty U_\infty^2)$. Domain duplicated.

the other hand, we have no clear explanation for the ‘pitchforking’ of the streaks, two arguments (at least) being plausible:

(i) oblique modes yielding ‘branchings’ or ‘defects’ in the streak system (see e.g. Comte, Lesieur, & Lamballais 1992, for analogous dislocations in mixing layers),

(ii) the frozen-fluid hypothesis (Taylor 1915), supported by the fact that pressure is quasi-uniform in the region of the ‘laminar-looking’ streaks (see figure 6): a fluid particle in a high-speed streak would thus propagate maintaining its velocity (i.e. positive u'_1 and negative u'_2) up to viscous damping, until it reaches the wall and creates a stagnation point.

In any case, figure 13 is clear evidence of the emergence of a purely spanwise (i.e. independent of time) unstable mode, in a region where the velocity profile starts becoming turbulent without any hairpin vortex being formed or ejected yet.

4.3. The early-transitional state

We recall that the eigenmode \hat{U} we use for the upstream forcing corresponds to the most amplified mode of the basic flow $U_{lam}(x_2)$ at $Re_\delta = 1000$, as predicted by the linear-stability theory within the temporal approximation (i.e. assuming streamwise periodicity). In the simulation, two-dimensional TS waves travel, as a whole, without noticeable amplification or damping, at the velocity $c \approx 0.35U_\infty$, which is not far from the phase speed $c_r = 0.321U_\infty$ of mode \hat{U} given by the aforementioned theory.

The signature of these waves on the pressure field at the wall is shown in figure 14,

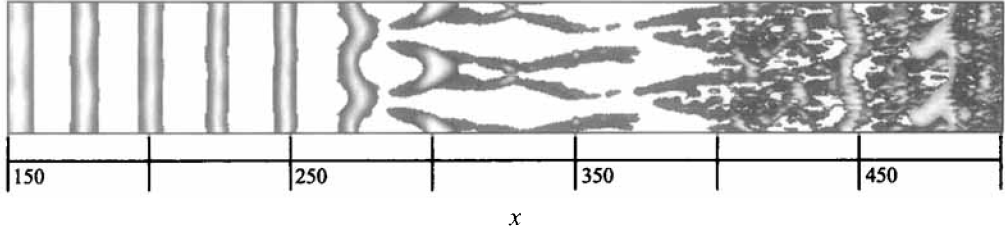


FIGURE 15. Top view of the transitional zone showing the isosurfaces $\omega_1 = \pm 0.1U_\infty/\delta_i$ (in black) and, in grey, $p = 0.999 p_\infty \approx p_\infty - 0.006 (\frac{1}{2}\rho_\infty U_\infty^2)$. Domain duplicated.

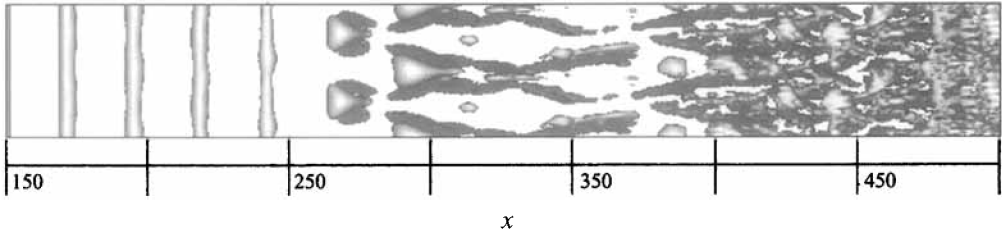


FIGURE 16. Same view as figure 15, but with the isosurface $u_2 = 0.007U_\infty$ (grey) instead of the low-pressure isosurface. Domain duplicated.

together with an isosurface of low pressure which will be commented upon later. This figure is essentially relevant to the laminar stage of the flow, for which the pressure extrema are at the wall (see figure 6). From $250\delta_i$ to $320\delta_i$, we can see the emergence of an oblique sub-harmonic mode, although only one half of its spanwise period is actually simulated. We will try to show later that this is a mode of secondary instability (of the H-type, after Herbert 1988) and not, for example, an oblique TS wave. In any case, we see clearly the formation of Λ -shaped structures of low pressure, arranged in a staggered pattern. In contrast, the high pressures lose momentarily their spatial organization. Note that we can only see half a streamwise period of this oblique sub-harmonic instability (i.e. one TS period). Figure 15 shows weak streamwise vorticity (of the order of one tenth of the spanwise vorticity at the wall), which appears on the legs of the Λ -shaped structures of low pressure. This might contribute to the disruption of the high-pressure structures. Figure 16 shows, for the same transition zone, the longitudinal vorticity as well as the positive vertical velocity at a very low threshold. Before transition, the fluid rises upstream of the Λ -shaped low-pressure rollers. During transition, fluid originating from the near-wall region is pumped between their legs. The isosurfaces of vertical velocity, previously organized in purely spanwise stripes on the edge of the two-dimensional TS billows, follow the spatial organization of the streamwise vorticity during the transition.

Another picture of the early-transitional region is given in figure 17 (see page 17), which shows isosurfaces of low and high pressures cut by a map of ω'_3 at $x_3 \simeq 20\delta_i$. The amplitude of the TS pressure fluctuations decreases smoothly at a constant phase when the distance to the wall increases. This is why our isobaric surfaces have the shape of arches, which are initially two-dimensional. In contrast, because of the adherence condition at the wall, a perturbation of spanwise vorticity at any height will induce a perturbation of the opposite sign at the wall. The change of sign occurs at the critical layer x_{2c} for which $u_1(x_{2c}) = c_r$, the phase speed of the TS waves: under the low-pressure arches are found negative vorticity fluctuations (i.e. an

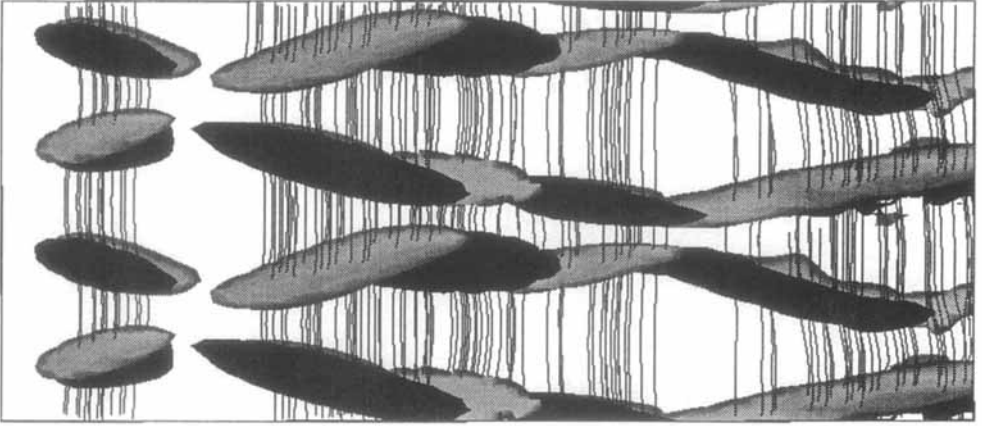


FIGURE 18. Top view for $260\delta_i \leq x \leq 373\delta_i$; isosurfaces $\omega_1 = 0.1U_\alpha\delta_i$ (grey) and $\omega_1 = -0.1U_\alpha\delta_i$ (dark), together with the most three-dimensional vortex lines in this region. Domain duplicated.

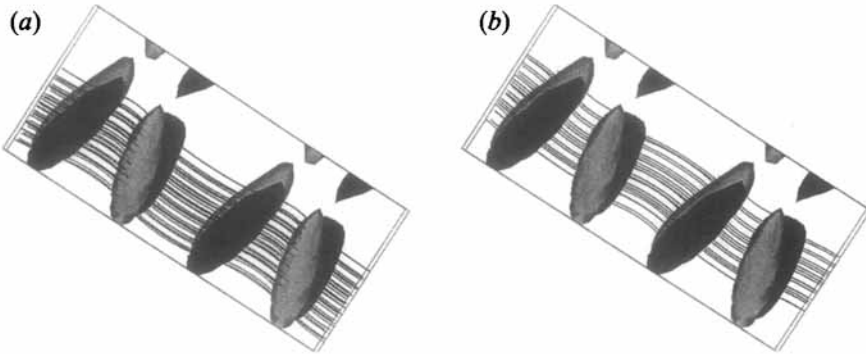


FIGURE 19. Magnification of the leftmost part of figure 18, $x_1/\delta_i \in [260, 291]$, with more vortex lines, above and below the critical layer (left and right plots, respectively). Domain duplicated.

increase of $|\omega_3|$). The converse is observed in the high-pressure arches. The further three-dimensionalization appears in the figure through the streamwise stretching of the ω_3 contours through the isobaric arches, at an angle with respect to the wall which is of about 5° . Figure 18 confirms that the streamwise stretching of vorticity is weak: the lines shown originate from the points where $|\omega_1|$ is the highest in the portion of the domain considered. These lines are nevertheless hardly three-dimensionalized yet. Let us now focus on the region between $260\delta_i$ and $291\delta_i$ (figure 19), distinguishing between the lines located above and below the critical layer. As expected, the lines above the critical layer are (slightly) stretched towards the positive x_1 in between the legs of the A-shaped structures. Below x_{2c} , they wave 180° out of phase.

We now provide some data supporting the idea that the transition in our spatially growing calculation begins with the growth of a sub-harmonic mode of secondary instability (H-type transition). Within this framework, the basic state consists of a self-similar Blasius profile, onto which constant-amplitude TS waves are superimposed. This is verified in our simulation up to $x_1 \approx 250\delta_i$, after which the velocity profile starts changing. The solid line in figure 20 shows the streamwise evolution of a

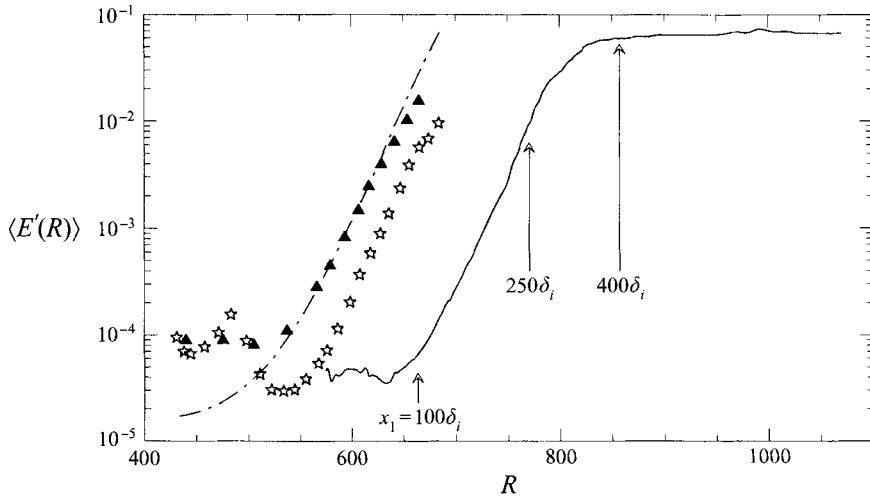


FIGURE 20. Amplification curves for $\langle E' \rangle$ (solid line), the subharmonic mode in Kachanov & Levchenko (1984, stars and triangles for the ‘unprimed’ and ‘primed’ cases, respectively) and in Herbert *et al.* (1986, dashed line).

time-averaged r.m.s. measure of three-dimensionality,

$$\langle E' \rangle(R) = \left[\frac{1}{U_\infty^2 T L_3 L_2} \int_0^T \int_0^{L_3} \int_0^{L_2} \left\| \mathbf{u}(\mathbf{x}, t) - \frac{1}{L_3} \int_0^{L_3} \mathbf{u}(\mathbf{x}, t) dx_3 \right\|^2 dx_2 dx_3 dt \right]^{1/2}, \quad (4.4)$$

as a function of $R = Re_{x_1}^{1/2}$ which is proportional to the local displacement thickness of the layer given by the Blasius laminar self-similar spreading law (3.1). The series of symbols shows the growth of the r.m.s. amplitude of the subharmonic mode, measured by Kachanov & Levchenko (1984) in two slightly different cases: one with a ribbon vibrating at the fundamental only (stars), the other with a ribbon also vibrating around the subharmonic (‘primed’ case, triangles). The dashed line shows the growth of an H-mode predicted by the secondary-stability theory (Herbert, Bertolotti & Santos 1986) in the latter case. All these curves display a subrange with approximately exponential growth, at a rate $\gamma_r = d[\ln \langle E' \rangle] / dR \approx 1.5 \times 10^{-2}$, the different ‘amplitudes’ being of the same order of magnitude. This suggests that the growth of $\langle E' \rangle$ is mostly due to an H-mode, although detuned modes may also be present as in the ‘primed’ case of Kachanov & Levchenko (1984).

The offsets between the curves certainly come from the forcings, although they are sufficiently similar to make this comparison relevant: in Kachanov & Levchenko (1984), the r.m.s. amplitude of the TS forcing is $A = 0.44\%$ and the frequency parameter $F = 10^6(2\pi/\lambda_{TS})c_r(v/U_\infty^2) = 124$, whereas we have in our case $A = 0.35\%$ and $F = 105$. For such small amplitudes (i.e. $A < 5 \cdot 10^{-3}$), secondary-stability theory (Santos & Herbert, 1986), confirmed by experiments (Thomas 1987) find “a broad peak of amplification for detuned modes in the neighbourhood of the subharmonic mode” (Herbert 1988), the fundamental mode of secondary instability being damped. Note that branch II of the Blasius stability diagram is crossed at $R = 606$ in for $F = 124$ and at $R \approx 700$ for $F = 105$, without any visible effect on γ_r . This confirms that, as Herbert (1988) said, “modes of secondary instability and oblique TS modes are two different kinds of animals”.

As mentioned by a referee, a detailed comparison of the growth rates of the separated leading modes would be necessary to conclude whether the subharmonic secondary instability has been properly captured. This has been done by Thumm *et al.* (1989) in a DNS of transition in a compressible spatially developing boundary layer. We have also carried out DNS of our weakly-compressible spatial boundary layer, at the same conditions (resolution, boundary conditions) as the LES: the DNS blows up during the early stage of transition, but before this happens predicts results in very good agreement with the LES. This is a further argument that our subgrid model is inactive during this stage, which was the required aim.

To complete discussion of the transition process, let us come back to the range $300\delta_i \lesssim x_1 \lesssim 400\delta_i$, immediately downstream of the subharmonic transitional region, where figure 13 shows laminar-looking longitudinal low- and high-speed streaks. Figure 14 also shows that the pressure is quasi-uniform in this region. This is reminiscent of the exact solution to the Euler equations in a constant shear at uniform pressure (in an unbounded domain) proposed in Métais *et al.* (1992). This solution consists of ‘vertical’ slices of fluid, parallel to the flow direction. They move vertically at a constant velocity, and their longitudinal perturbed velocity is proportional to t . Their perturbed velocity, with respect to the basic flow $\bar{u}(x_2)$, is given by

$$\left. \begin{aligned} u'_1(x_3, t) &= u'_{1_0}(x_3) - \frac{d\bar{u}_1}{dx_2} U'_{2_0}(x_3) t, \\ u'_2(x_3, t) &= u'_{2_0}(x_3), \\ u'_3(x_3, t) &= 0, \end{aligned} \right\} \quad (4.5)$$

where $u'_{2_0}(x_3)$ is arbitrary, $u'_{1_0}(x_3)$ being either zero or proportional to u'_{2_0} . This solution can be generalized to viscous flows in the case $u'_{2_0}(x_3) \propto \sin(\beta x_3)$. The perturbed velocity then reads

$$\left. \begin{aligned} u'_1(x_3, t) &= \left[u'_{1_0}(x_3) - \frac{d\bar{u}_1}{dx_2} U'_{2_0}(x_3) t \right] \exp(-\nu\beta^2 t), \\ u'_2(x_3, t) &= u'_{2_0}(x_3) \exp(-\nu\beta^2 t) \\ u'_3(x_3, t) &= 0. \end{aligned} \right\} \quad (4.6)$$

Of course, it is still assumed that $d\bar{u}_1/dx_2$ is a constant (which is acceptable close to the wall), and the adherence condition at the wall is not accounted for, which is highly questionable. Notice also that these solutions which, initially, grow linearly

FIGURE 21. (a) Isosurface $p = 0.990$ $p_x \approx p_x - 0.057 (\frac{1}{2}\rho_x U_x^2)$, plus 100 vortex lines passing through it, coloured by their local vorticity magnitude. Perspective view. (b) Same as (a) but from the side.

FIGURE 22. (a) Magnification of the domain showing: isosurfaces $\omega_1 = 0.15U_x/\delta_i$ (green) and $-0.15U_x/\delta_i$ (white); vortex lines coloured by the vorticity magnitude (colourmap on the right), passing through points between 520 and $550\delta_i$; map at constant x_3 of the spanwise vorticity ω_3 , associated to the colourmap on the left. Domain duplicated. (b) Same as (a) but showing the whole domain.

(a)

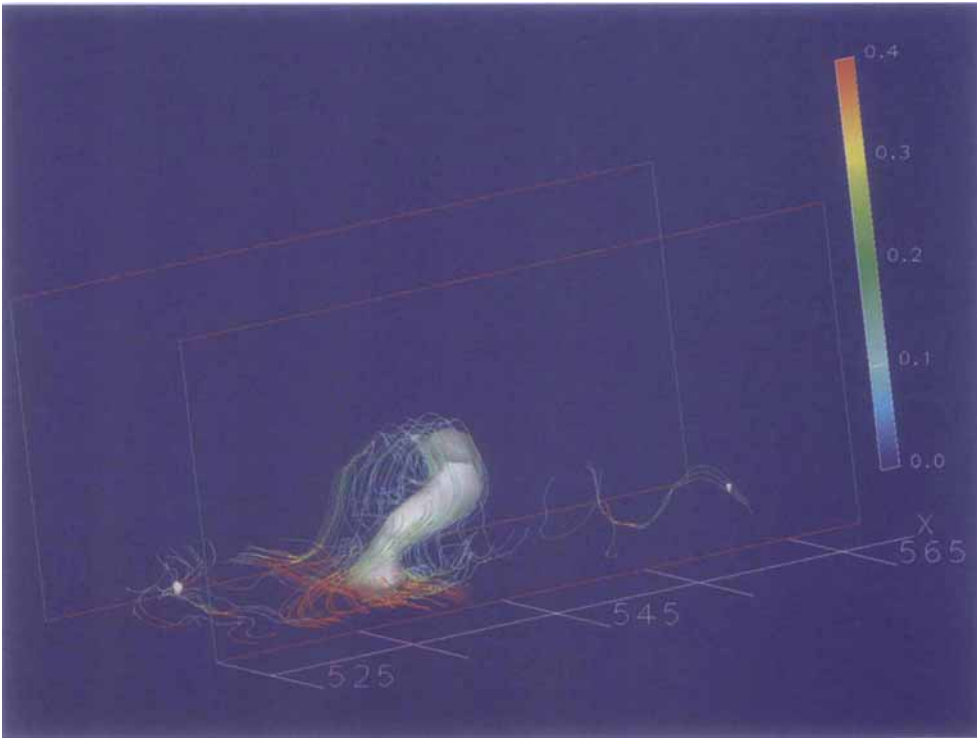


FIGURE 21(a). For caption see page 25.

(a)

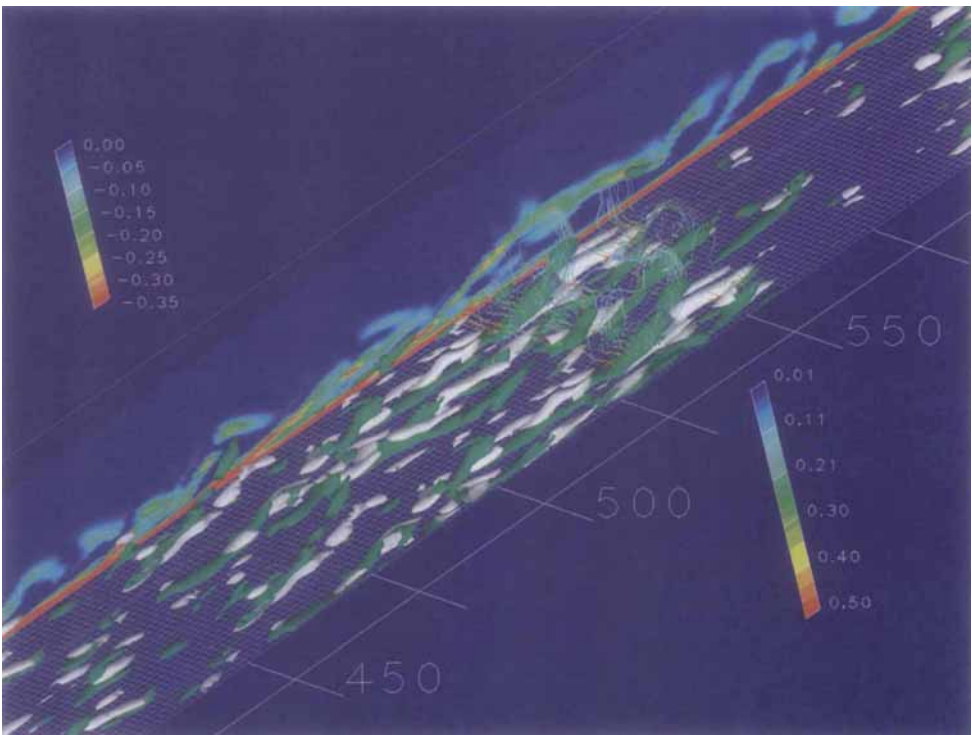


FIGURE 22(a). For caption see page 25.

(b)

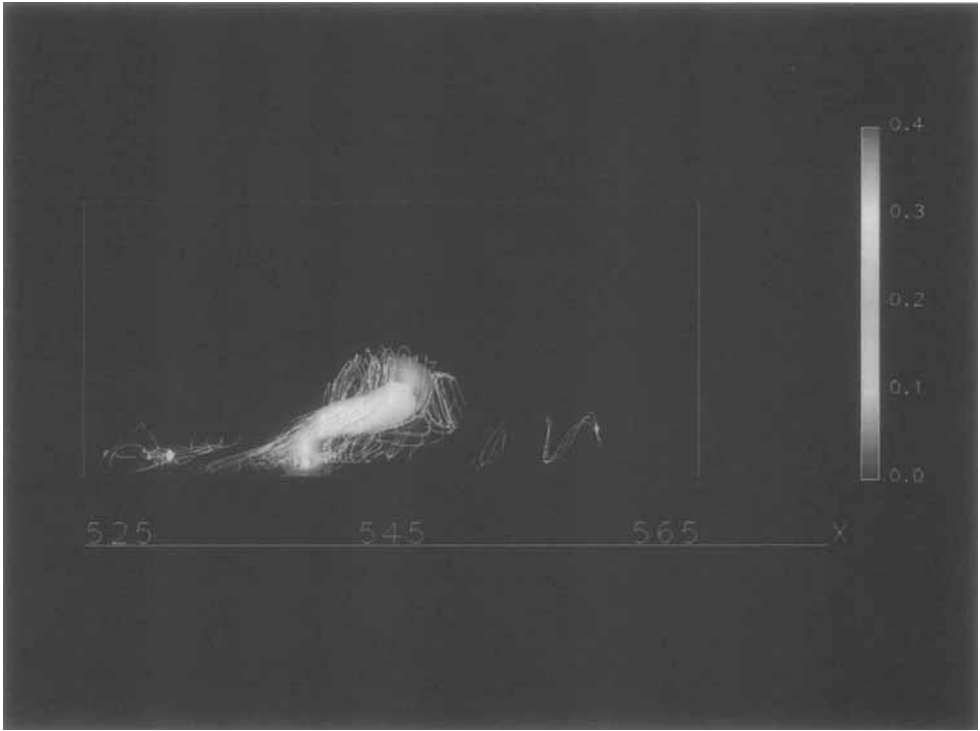


FIGURE 21(b). For caption see page 25.

(b)

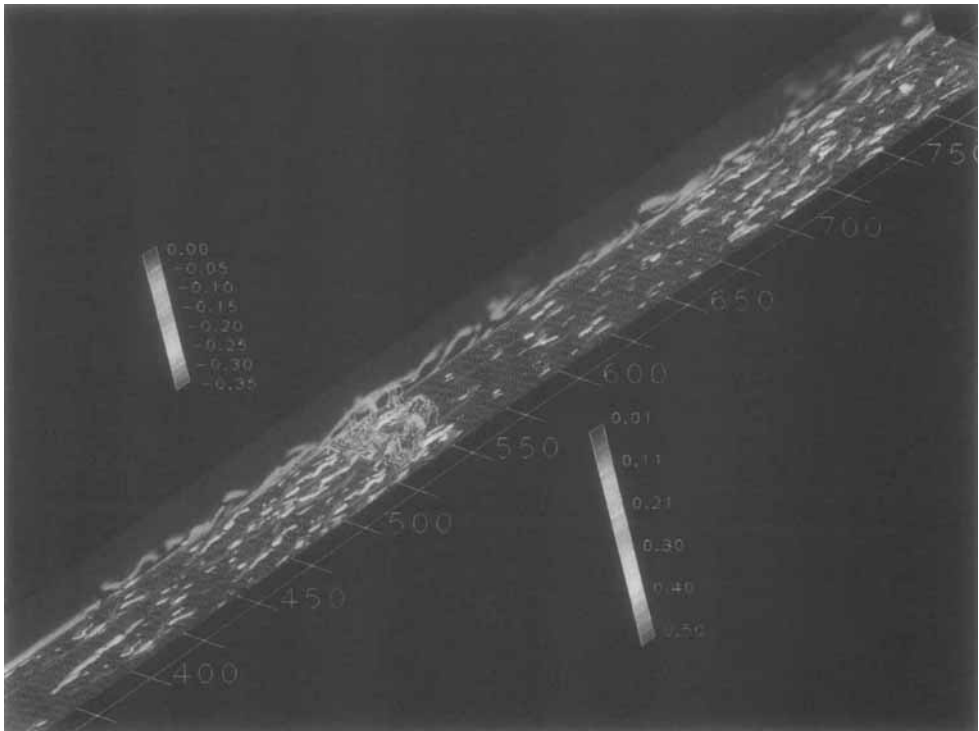


FIGURE 22(b). For caption see page 25.

with time, have certain analogies with the algebraic instabilities proposed by Landahl (see e.g. Landahl & Mollo-Christensen 1992, pp. 115–122).

4.4. *The late-transitional and turbulent states*

This covers all the domain from $x_1 = 400\delta_i$ onwards. We will first present visualizations of the flow, and then instantaneous or statistical data.

4.4.1. *Visualizations*

In the region we are now looking at, the lowest pressures are recorded away from the wall. The isosurface in figure 14 shows a region of intense activity around $x_1 = 550\delta_i$ (i.e. $Re_{x_1} = 0.88 \times 10^6$) involving hairpin vortices. A close-up of the strongest is shown in figure 21. This is, in fact, a one-legged hairpin vortex, the branch for which the vorticity vector points downstream (i.e. the one into which ω_1 is positive) being the strongest. Note that it involves only vortex lines relatively far away from the wall, the lines below having a higher circulation and remaining fairly two-dimensional. Consequently, the vorticity magnitude is only of the order of $0.1U_\infty/\delta_i$ in the legs and tips of the hairpin vortex, whereas the mean spanwise vorticity at the wall, $-u_t^2/\nu$, is here $\approx -1.5U_\infty/\delta_i$. We note from the side view that the vortex lines are inclined at about $20^\circ - 25^\circ$ with respect to the wall, except at the tip of the vortex where they are kinked approximately vertically, probably because of self-induction. The low-pressure isosurface follows, except close to the wall where we have locally $\partial p/\partial x_2 \simeq 0$.

Zooming out, figure 22 shows that there is in fact a streamwise alignment of vortex lines having hairpin shape, the concentration into tubes as in the previous figure occurring only locally. This streamwise coherence is emphasized by a map of spanwise vorticity in a peak plane. It shows ‘braids’ being stretched at angles with respect to the wall ranging between 10° and 60° , with a maximum of probability apparently lower than 45° . Zooming out again and looking downstream, we can see several such braids in the same peak plane, with detachment of vorticity which is tempting to interpret in terms of local mixing layers, ejections and bursting events: indeed, in almost all detached zones, we can see a local concentration of vorticity corresponding to the tip of a hairpin vortex, with, immediately downstream, weaker spanwise vorticity with little spanwise organization. Although, here again, our resolution is too low to be conclusive, we think that this vorticity corresponds to local mixing layers detached from the tip of the hairpins, as in the classical interpretations. This point of view is bolstered by the inflectional allure of the local velocity profiles (such as figure 10*b*), which seems sufficiently persistent in space and time to be significant and yield Kelvin–Helmholtz instability.

Between $575\delta_i$ and $675\delta_i$, we see less streamwise vorticity near the wall, but about as many ejections and hairpin vortices as anywhere else in the turbulent region. This is visible in figure 23, where we can also see a map of u'_1 at $x_1 = 612\delta_i$, showing that the height of the streaks is commensurate with that of the hairpins. However, as mentioned in the discussion of figures 8 and 9 (page 18), the extremes of u'_1 lie lower, in the buffer region, which is confirmed by figure 24, for which the isosurface level is larger, in magnitude, than the contour shown at $x_1 = 612\delta_i$. As in the transitional regime, we interpret the fact that these extremes are close to the wall as evidence that the source of the peak-and-valley splitting lies even closer to the wall.

The fact that the hairpins are stretched at an angle, with respect to the wall, which is less than 45° has so far prevented us from finding simple convincing analytical models. Moreover, there is a factor of about 10 between vorticity in the near-wall region and

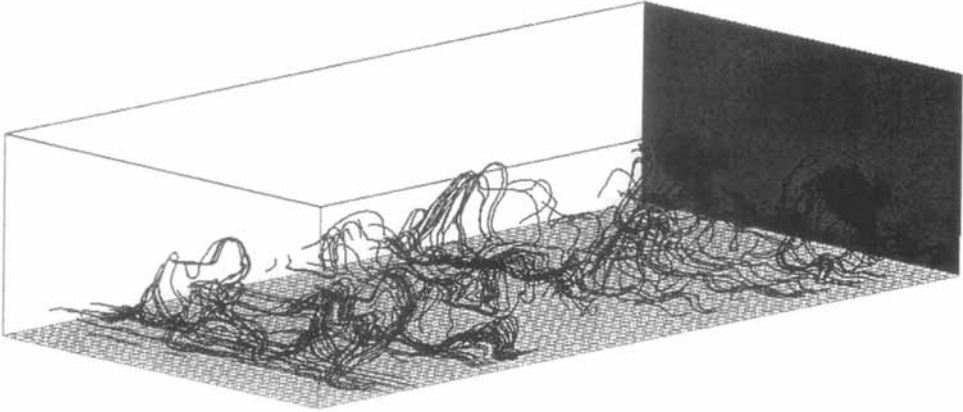


FIGURE 23. Perspective view of region $x/\delta_i \in [524, 612]$, showing vortex lines plus a vertical slice of u'_1 at $x_1 = 612\delta_i$. Domain duplicated.

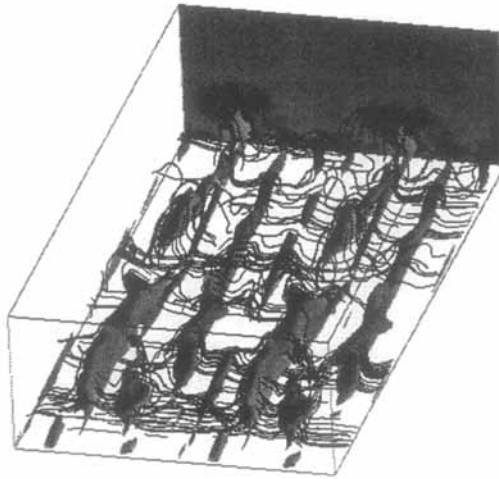


FIGURE 24. Same as in figure 23 but from another viewpoint, showing also the isosurface $u'_1 = -0.017U_\infty$. Domain duplicated.

that in the outer region, the interaction between these regions remaining unclear to us. If we accept that the hairpins form by stretching of relatively weak vorticity in the logarithmic or wake regions, possibly by some ‘rapid-distortion’ mechanism (Townsend 1976), we also have to accept the existence of another mechanism, closer to the wall, involving larger vorticities. Among the candidates are purely longitudinal alternate vortices at the wall (Blackwelder & Eckelmann 1979), from which the hairpins would stem. The reader is referred to Robinson (1991) for review. The numerical work of Hamilton, Kim & Waleffe (1995) concerning turbulent plane Couette flow supports this interpretation. We have not seen such vortices (the vortex lines closest to the wall being spanwise, as in the transitional regime). Instead, we

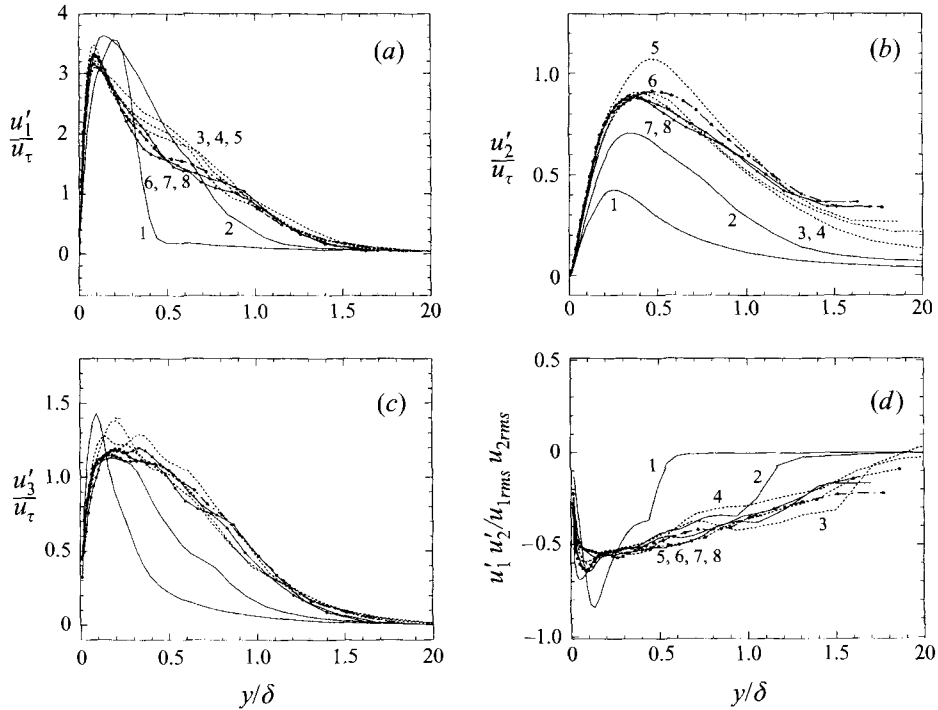


FIGURE 25. Transverse evolution of the r.m.s. velocities u'_i/u_τ and the Reynolds stresses for eight streamwise positions: $10^{-3}Re_x$ equal to 640 (curve 1), 735 (2), 830 (3), 890 (4), 955 (5), 1020 (6), 1080 (7), 1143 (8). The first two positions are marked with solid lines, the next three with dashed lines and the last three with points. δ stands here for the boundary layer thickness δ_{99} .

still see the spanwise modulation of the vorticity at the wall that we mentioned in the previous section. We therefore conjecture that the same purely spanwise (i.e. independent of time) mode has survived transition, and that it now essentially concerns the viscous sub layer.

4.4.2. Turbulent fluctuations

We plot on figure 25 the time- and-spanwise-averaged r.m.s. velocity profiles $u'_{i,rms}$ and the Reynolds stresses for eight streamwise positions. All quantities collapse onto a turbulent profile from $x_1 = 500\delta_i$ (i.e. $Re_{x_1} = 0.8 \times 10^6$, curve 3 in figure 25) onwards. A comparison with experimental and numerical findings is given in figure 26 for the turbulent profiles. For this figure, we recall experimental data of Eckelmann (1970) reported in Gilbert & Kleiser (1988) (velocity fluctuation profiles in a turbulent channel flow) obtained for a friction velocity u_τ equal to $0.042U_\infty$. A very good agreement is observed for the streamwise velocity whereas we notice some discrepancies in the vertical and spanwise velocities. The same remarks apply to the comparison with the DNS of Spalart (1988). The under-evaluation of the vertical and spanwise fluctuation velocities is often observed in numerical simulations, even for DNS. This point is discussed in Antonia *et al.* (1992), who invoked the higher resolution needed for the longitudinal velocity.

The Reynolds stresses normalized by the product of streamwise and transverse r.m.s. velocities are shown in figure 25(d). They grow during transition and accumulate in a turbulent profile, showing that the boundary layer has reached a self-similar state. The

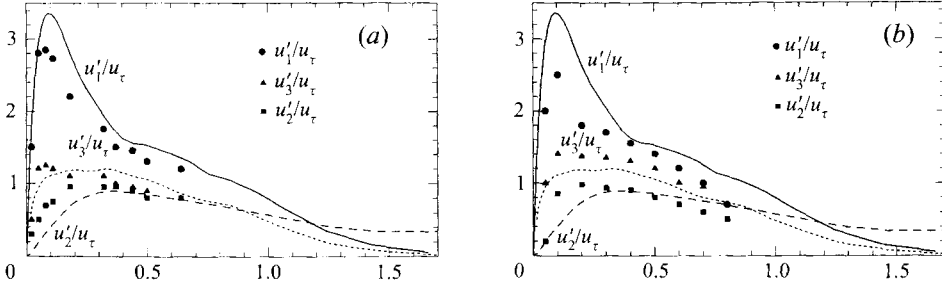


FIGURE 26. (a) R.m.s. velocity fluctuations u'_i/u_τ for $Re_x \approx 10^6$, as a function of x_2/δ together with experimental results of Eckelmann in turbulent channel flow for $Re_\tau = 209$ (symbols), δ stands here for the boundary layer thickness δ_{99} (for our simulation, we evaluate the equivalent $Re_\tau \approx 300$). (b) Same fluctuation profiles together with the DNS of Spalart (1988) for $Re_\theta = 1470$, that is $Re_\delta \approx 2000$.

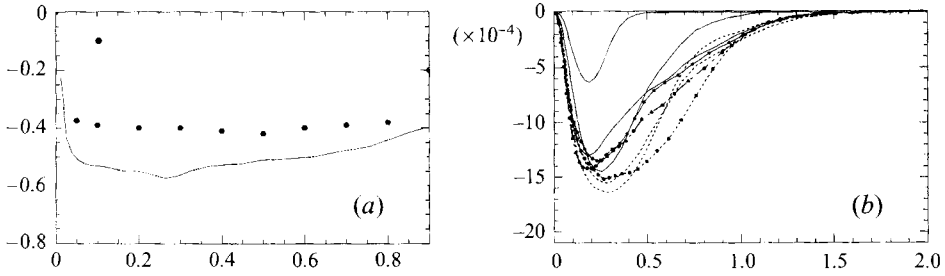


FIGURE 27. (a) Reynolds stresses $u'_1 u'_2 / u_{1,rms} u_{2,rms}$ as a function of x_2/δ , against the experimental results of Sabot & Comte-Bellot (1976) reported in Moin & Kim (1982); (b) $u'_1 u'_2 / U_\infty^2$ as a function of x_2/δ for the same streamwise positions as figure 25.

last normalized profile shows a plateau in fairly good agreement with the experiments of turbulent channel flow on Sabot & Comte-Bellot (1976) (figure 27a). Figure 27(b) shows the non-normalized Reynolds stress profiles. For example, at $Re_x = 10^6$, i.e. $Re_{\delta_1} \approx 2000$, the peak $u'_1 u'_2 \approx -14 \times 10^{-4} U_\infty^2$ is reached at $y \approx 0.17 \delta_1$, i.e. ≈ 12 wall units. This is consistent with temporal DNS at higher resolution, in particular the ones performed by Ducros (1995) with the same code.

4.4.3. Eddy viscosity

We plot isosurfaces of the eddy viscosity given by the FS model (figure 28) and the FSF model (figure 29) together with isosurfaces of vertical velocity u_2 . The threshold is very low, one third of the molecular viscosity. As expected from §2, our model gives lower viscosity than the FS model, which is sensitive to the three-dimensionalization of TS waves at the beginning of transition, where the big Λ -vortices form. At the turbulent stage, we plot on figure 30 isosurfaces of the eddy viscosity given by the FSF³ model for the same part of the domain as in figure 24. The threshold is now eleven times the molecular viscosity. Our FSF model gives high eddy viscosities in the head and legs of the hairpin vortices, that is where high vorticity fluctuations are reached and small structures are generated.



FIGURE 28. Top view of the region $x_1/\delta_t \in [150, 450]$ showing the isosurfaces $u_2 = 0.007U_\infty$ (grey) and, in dark, $\mu_t = 0.33\mu(T_\infty)$ given *a priori* by the SF model. Domain duplicated.



FIGURE 29. Same view as figure 28, but with the dark isosurface $\mu_t = 0.33\mu(T_\infty)$ given by the FSF³ model. Domain duplicated.

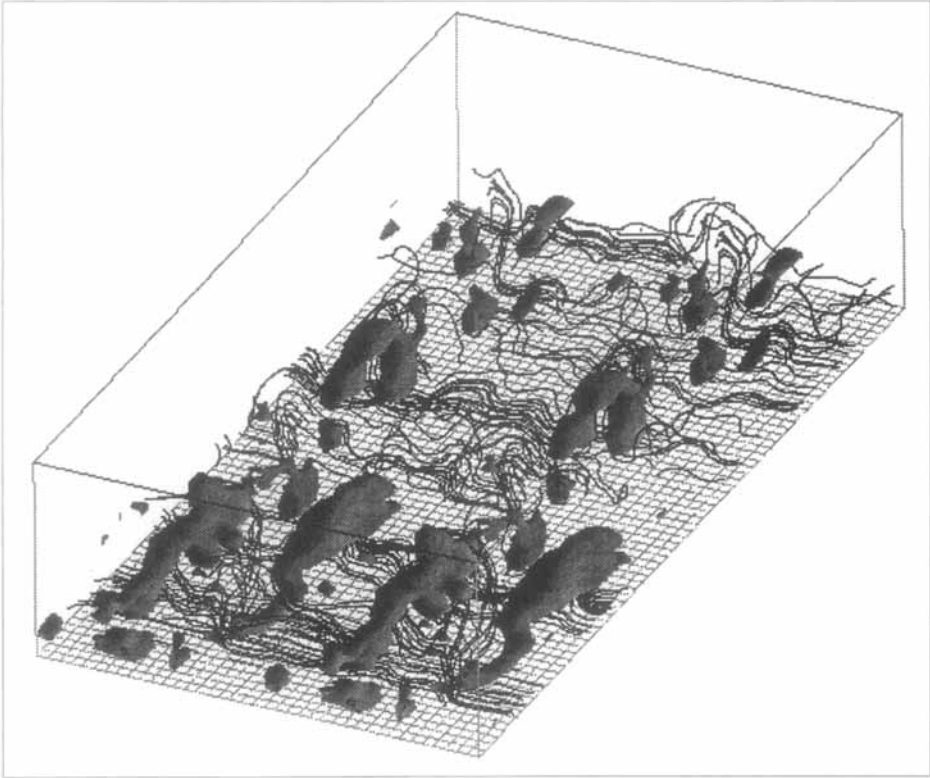


FIGURE 30. Perspective view showing the same vortex lines as in figures 23 and 24, plus the isosurface $\mu_t = 11\mu(T_\infty)$ given by the FSF³ model. Domain duplicated.

5. Conclusions

We have performed a large-eddy simulation of the complete transition to turbulence in a quasi-incompressible boundary layer, developing spatially above an adiabatic flat plate, with weak perturbations superposed upon the laminar upstream profile. This problem cannot be tackled with classical subgrid models such as Smagorinsky's or the

structure-function model, which relaminarize the flow. Its solution requires prohibitive computing resources (more than 800 hours on a CRAY YMP) if one wants to use direct-numerical simulations.

To solve the problem, we have reformulated the structure-function model (SF), expressing the local kinetic-energy spectrum in terms of the second-order structure function of the velocity field filtered with the aid of a discretized Laplacian iterated three times. This eliminates large-scale oblique perturbations of the flow, which turn out to be responsible for a too high SF eddy viscosity when transition starts developing.

This so-called filtered structure-function model (FSF) was used successfully to simulate the transition in a spatial boundary layer at Mach 0.5. The compressibility (inherent to the numerical method used), was chosen small enough to be negligible in the wall region. The computing time required by the LES is about ten times shorter than the DNS, which is a considerable improvement for further applications.

The transition starts with the three-dimensionalization of low pressure arches resulting from TS waves travelling at a velocity close to the phase velocity of the upstream perturbation. Big A -shaped low-pressure structures are produced, in a staggered pattern which is the signature of a subharmonic mode of secondary instability. Immediately downstream, a purely spanwise (i.e. time-independent) mode emerges from the near-wall region, with homogenization of pressure. It initiates peak-and-valley splitting over about the whole thickness of the layer, without evidence of turbulence yet, although the velocity profile starts changing. Pressure anomalies occur at the downstream end of the high-speed streaks. Shortly downstream ($\approx 500\delta_i$, i.e. $Re_{x_1} \approx 0.84 \times 10^6$), the flow has become turbulent, with persistence of the streak system. Our interpretation then globally corresponds to that of Klebanoff *et al.* (1962) and Kline *et al.* (1967), with the aforementioned spanwise mode as a main ingredient, which accounts for the stretching of hairpin vortices and the detachment of local mixing layers downstream of their tips. More precisely, the hairpin vortices which form in the simulation presented are made of vortex lines coming initially outside of the near-wall region. Consequently, they carry only about one tenth of the vorticity at the wall and are submitted only to moderate stretching.

Statistics of mean and r.m.s. velocities are provided: they display an error which does not exceed 30% with respect to experiments and related temporal DNS. The friction coefficient is in particular under-estimated. This is due both to the insufficient spanwise and transverse resolution in the near-wall region and to the fact that our subgrid-scale turbulence model remains slightly over-dissipative in the turbulent regime. However, the simulation provides all the known characteristics of transitional and turbulent boundary layers. For example, the type and growth rate of the prominent three-dimensional mode of secondary instability are well predicted.

To our knowledge, it is the first time that the LES of complete transition to turbulence in a spatially evolving boundary layer has been carried out with a low level of upstream forcing. The results presented are only qualitative (as noted by one referee), but their quality is sufficient to shed some light on the transition process. In particular, figures 13 and 20 suggest that the streaks result from nonlinear interactions (since $\langle E' \rangle$ has already started saturating where the streaks form) involving oblique subharmonic modes. However, the reason why such an interaction should result mostly in time-independent modes remains unclear unless one invokes algebraic instabilities (see e.g. Landahl & Mollo-Christiansen 1992). Because of their slow (spatial) growth, these time-independent instabilities are unlikely to generate the streaks directly, but they can resonate with the oblique subharmonic modes and drive

their nonlinear evolution. We are not aware of theoretical developments involving spatially growing modes of secondary instability and algebraic modes, but it should be possible to generalize the formalism thanks to which Benney & Gustavsson (1981) accounted for resonances between Orr–Sommerfeld and Squire modes. Note that, among the time-independent modes, is the so-called zero-zero mode which accounts for the change of shape of the mean velocity profile. With the present results, we cannot distinguish the respective roles played by this mode and the other time-independent modes in the breakdown to turbulence. All we can say is that the breakdown is observed at about $x_1 = 420\delta_i$, where: (a) the first ejection occurs (see figure 22), (b) the streaks become turbulent (figure 13), (c) the turbulent velocity profile is practically established (figure 2d).

The fact that (5) and (5) occur simultaneously somewhat simplifies the interpretation. We will nevertheless not speculate any further. New better-resolved simulations are in progress (all available datasets are accessible on request, including the present ones). We have also undertaken the same study in a high-Mach-number case ($M_\infty = 4.5$), starting upstream with Mack's second mode perturbed three-dimensionally. Preliminary results (Ducros 1995) indicate for the developed turbulent boundary layer a vortical structure very similar to the low-Mach-number case.

We would like to thank J. Ferziger, E. Lamballais, R. Gathmann, O. Métais and S. Prestemon for fruitful discussions, in particular on subgrid-scale modelling and streaks. This work was supported by CNES and Dassault Aviation (Hermès program) and by DRET. Computing time was provided by IDRIS and CCVR.

REFERENCES

- ADAMS, N. A. & KLEISER, L. 1993 Numerical simulation of transition in a compressible flat plate boundary layer. In *Transitional and Turbulent Compressible Flows*. ASME-FEX, vol. 151, pp. 101–110.
- ANTONIA, R. A., TEITEL, M., KIM, J. & BROWNE, L. W. B. 1992 Low-Reynolds-number effects in a fully developed channel flow. *J. Fluid Mech.* **236**, 579–605.
- BARTELLO, P., MÉTAIS, O. & LESIEUR, M. 1994 Coherent structures in rotating three-dimensional turbulence. *J. Fluid Mech.* **273**, 1–29.
- BACHELOR, G. K. 1953 *The Theory of Homogeneous Turbulence*. Cambridge University Press.
- BACHELOR, G. K., CANUTO, V. M. & CHASNOV, J. R. 1992 Homogeneous buoyancy-generated turbulence. *J. Fluid. Mech.* **235**, 325–349.
- BENNEY, D. J. & GUSTAVSSON, L. H. 1981 A new mechanism for linear and non-linear hydrodynamic instability. *Stud. Appl. Maths* **64**, 185–209.
- BLACKWELDER, R. F. & ECKELMANN, H. 1979 Streamwise vortices associated with the bursting phenomenon. *J. Fluid. Mech.* **94**, 577–594.
- CHOLLET, J.-P. & LESIEUR, M. 1981 Parameterization of small scales of three-dimensional isotropic turbulence utilizing spectral closures. *J. Atmos. Sci.* **38**, 2747–2757.
- COMTE, P., DUCROS, F., SILVESTRINI, J., DAVID, E., LAMBALLAIS, E., LESIEUR, M. & MÉTAIS, O. 1994 Simulation des grandes échelles d'écoulements transitionnels. *Proc. 74th. Fluid Dynamics AGARD Symp. Application of Direct and Large-Eddy Simulation to Transition and Turbulence', Chania, Crete, 18–21 April 1994*, pp. 14.1–14.12.
- COMTE, P., LESIEUR, M. & LAMBALLAIS, E. 1992 Large- and small-scale stirring of vorticity and a passive scalar in a 3-D temporal mixing layer. *Phys. Fluids A* **4**, 2761–2778.
- COUSTEIX, J. 1989 *Turbulence et Couche Limite*, p. 625. Cepadues.
- DEARDORFF, J. W. 1970 A three-dimensional numerical study of turbulent channel flow at large Reynolds numbers. *J. Fluid. Mech.* **41**, 453–480.
- DOMARADSKI, J. M., LIU, W. & BRACHET M. E. 1993 An analysis of subgrid-scales interactions in numerically simulated isotropic turbulence. *Phys. Fluids A* **7**, 1747–1759.

- DUCROS, F. 1995 Simulations numériques directes et des grandes échelles de couches limites compressibles. PhD thesis, INPG.
- DUCROS, F., COMTE, P. & LESIEUR, M. 1995 Direct and large-eddy simulations of a supersonic boundary layer. *Selected Proceedings of Turbulent Shear Flows 9*, pp. 283–300. Springer.
- ECKELMANN, H. 1970 Experimentelle Untersuchungen in einer turbulenten Kanalströmung mit starken viskosen Wandschichten. *MPI f. Strömungsforschung und AVA Göttingen Nr. 48*.
- FASEL, H. & KONZELMANN, U. 1990 Non-parallel stability of a flat-plate boundary layer using the complete Navier-Stokes equations, *J. Fluid Mech.* **221**, 311–347.
- FAVRE, A. 1965 Equations des gaz turbulents compressibles. *J. Méc.* **4**, 361–421.
- GERMANO, M., PIOMELLI, U., MOIN, P. & CABOT, W. 1991, A dynamic subgrid-scale eddy-viscosity model. *Phys. Fluids A* **3**, 1760–1765.
- GHOSAL, S., LUND, T. S., MOIN, P. & AKSEVOLL, K. 1995 A dynamic localization model for large-eddy simulation of turbulent flows. *J. Fluid Mech.* **286**, 229–255.
- GILBERT, N. & KLEISER, L. 1988 Near-wall phenomena in transition to turbulence. *Proc. Intl Seminar on Near-Wall Turbulence, Dubrovnik, Yugoslavia*.
- GONZE, M. A. 1993 Simulation numérique des sillages en transition à la turbulence. PhD thesis, INPG.
- GUO, Y., ADAMS, N. A. & KLEISER, L. 1995 Modeling of non-parallel effects in temporal direct numerical simulations of compressible boundary-layer transition. *Theor. Comput. Fluid Dyn.* **7**, 141–157.
- HALL, A. A. & HISLOP, G. S. 1938 Experiments on the transition of the laminar boundary layer on a flat plate. *Aero. Res. Council, London, RM 1843*.
- HAMILTON, J. M., KIM, J. & WALEFFE, F. 1995 Regeneration mechanisms of near-wall turbulence structure *J. Fluid Mech.* **287**, 317–348.
- HERBERT, T. 1988 Secondary instability of boundary layers. *Ann. Rev. Fluid Mech.* **20**, 487–526.
- HERBERT, T., BERTOLOTI, F. P. & SANTOS, G. R. 1986 Floquet analysis of secondary instability in shear flows. In *Stability of Time-Dependent and Spatially Varying Flows*. (ed. D. L. Dwoyer & M. Y. Hussaini), pp. 43–57. Springer.
- JIMENEZ, J. & MOIN, P. 1991 The minimal flow unit in near-wall turbulence. *J. Fluid Mech.* **225**, 213–240.
- JOSLIN, R. D., STREETT, C. L. & CHANG C. L. 1993 Spatial direct numerical simulation of boundary-layer transition mechanisms: validation of PSE theory. *Theor. Comput. Fluid Dyn.* **4**, 271–288.
- KACHANOV, YU. S. & LEVCHENKO, V. YA. 1984 The resonant interaction of disturbances at laminar-turbulent transition in a boundary layer. *J. Fluid Mech.* **138**, 209–247.
- KLEBANOFF, P. S., TIDSTROM, K. D. & SARGENT, L. M. 1962 The three-dimensional nature of turbulent boundary layer instability. *J. Fluid Mech.* **12**, 1–34.
- KLEISER, L. & ZANG, T. A. 1991 Numerical simulation of transition in wall-bounded shear flows. *Ann. Rev. Fluid Mech.* **23**, 495–537.
- KLINE, S. J., REYNOLDS, W. C., SCHRAUB, F. A. & RUNSTADLER, P. W. 1967 The structure of turbulent-boundary layers. *J. Fluid. Mech.* **30**, 741–773.
- KRAICHNAN, R. H. 1976 Eddy viscosity in two and three dimensions. *J. Atmos. Sci.* **33**, 1521–1536.
- LAMBALLAIS, E., LESIEUR, M. & MÉTAIS, O. 1996 Effects of spanwise rotation on the vorticity stretching in transitional and turbulent channel flow. *Intl J. Heat and Fluid Flow*, **17**.
- LANDAHL, M. T. & MOLLO-CHRISTENSEN, E. 1992 *Turbulence and Random Processes in Fluid Mechanics*, 2nd Edn. Cambridge University Press.
- LESIEUR, M. 1990 *Turbulence in Fluids*, 2nd Edn. Kluwer.
- LESIEUR, M., COMTE, P. & MÉTAIS, O. 1995 Numerical simulation of coherent vortices in turbulence, *Appl. Mech. Rev.* **48**, 121–149.
- LESIEUR, M. & ROGALLO, R. 1989 Large-eddy simulation of passive scalar diffusion in isotropic turbulence. *Phys. Fluids A* **1**, 77–95.
- MÉTAIS, O. & LESIEUR, M. 1992 Spectral large-eddy simulation of isotropic and stably stratified turbulence. *J. Fluid Mech.* **239**, 157–194.
- MÉTAIS, O., YANASE, S., FLORES, C., BARTELLO, P. & LESIEUR, M. 1992 Reorganization of coherent vortices in shear layers under the action of solid-body rotation. In *Turbulent Shear Flows*, pp. 414–430. Springer.
- MOIN, P. & KIM, J. 1982 Numerical investigation of turbulent channel flow. *J. Fluid Mech.* **118**, 341–377.

- MURLIS, J., TSAI, H. M. & BRADSHAW, P. 1982 The structure of turbulent boundary layer at low Reynolds numbers. *J. Fluid Mech.* **122**, 13–56.
- NORMAND, X. & LESIEUR, M. 1992 Direct and large-eddy simulation of transition in the compressible boundary layer. *Theor. Comput. Fluid Dyn.* **3**, 231–252.
- PRUETT, C. D. & ZANG, T. A. 1992 Direct numerical simulation of laminar breakdown in high-speed, axisymmetric boundary layers. *Theor. Comput. Fluid Dyn.* **3**, 345–367.
- RAI, M. M. & MOIN, P. 1993 Direct numerical simulation of transition and turbulence in a spatially evolving boundary layer. *J. Comput. Phys.* **109**, 169–192.
- ROBINSON, S. K. 1991 Coherent motions in the turbulent boundary layer. *Ann. Rev. Fluid Mech.* **23**, 601–639.
- SABOT, J. & COMTE-BELLOT, G. 1976 Intermittency of coherent structure in the core region of fully developed turbulent pipe flow. *J. Fluid Mech.* **74**, 767–796.
- SANTOS, G. R. & HERBERT, T. 1986 Combination resonance in boundary layers. *Bull. Am. Phys. Soc.* **31**, 1718.
- SCHLICHTING, H. 1987 *Boundary Layer Theory*, reissue of 7th Edn. McGraw Hill.
- SILVEIRA, N., GRAND, D., MÉTAIS, O. & LESIEUR, M. 1993 A numerical investigation of the coherent structures of turbulence behind a backward-facing step. *J. Fluid Mech.* **256**, 1–25.
- SILVESTRINI, J. H., COMTE, P. & LESIEUR, M. 1995 DNS and LES of incompressible mixing layers developing spatially. *10th Symp. on Turbulent Shear Flows, University Park, USA, Aug. 14–16*.
- SMAGORINSKY, J. 1963 General circulation experiments with the primitive equations, I: The basic experiment. *Mon. Weather Rev.* **91**, 99–163.
- SPALART, P. R. 1988 Direct simulation of a turbulent boundary layer up to $R_\theta = 1410$. *J. Fluid Mech.* **187**, 61–98.
- SPALART, P. R. & YANG, K. S. 1987 Numerical study of ribbon-induced transition in Blasius flow. *J. Fluid Mech.* **178**, 345–365.
- TAYLOR, G. I. 1915 Eddy motion in the atmosphere. *Phil. Trans. R. Soc. Lond. A* **215**, 1–26.
- THOMAS, A. S. W. 1987 Experiments on secondary instabilities in boundary layers. *Proc. US Natl. Congr. Appl. Mech., 10th, Austin, Tex.* pp. 436–444. ASME.
- THOMPSON, K. W. 1987 Time dependent boundary conditions for hyperbolic systems. *J. Comput. Phys.* **68**, 1–24.
- THUMM, A., WOLZ, W. & FASEL, H. 1989 Numerical simulation of spatially growing three-dimensional waves in compressible boundary layers. *Third IUTAM Symp. Laminar-Turbulent Transition, Toulouse, 11–15 septembre 1989* (ed. D. Arnal & R. Michel), pp. 303–308. Springer.
- TOWNSEND, A. A. 1976 *The Structure of Turbulent Shear Flow*, 2nd Edn. Cambridge University Press.
- VOKE, P. R. & YANG, Z. 1993 Numerical studies of the mechanisms of bypass transition in the flat plate boundary layer. *Proc. Turbulent Shear Flows 9, Kyoto*.
- YANG, Z. & VOKE, P. 1993 Large-eddy simulation of transition under turbulence. *Rep. ME-FD/93.12*, Dept Mech. Eng., University of Surrey.
- YOSHIZAWA, Y. 1986 Statistical theory for compressible turbulent shear flows, with the application to subgrid modelling. *Phys. Fluids* **29**, 2152–2164.